Nonperturbative renormalization of quark bilinear operators and B_K using domain wall fermions

Y. Aoki,[1] P. A. Boyle,[2] N. H. Christ,[3] C. Dawson,[1,*] M. A. Donnellan,[4] T. Izubuchi,[1,5] A. Jüttner,[4] S. Li,[3] R. D. Mawhinney,[3] J. Noaki,[6] C. T. Sachrajda,[4] A. Soni,[7] R. J. Tweedie,[2] and A. Yamaguchi[8]

(RBC and UKQCD Collaborations)

[1]*RIKEN-BNL Research Center, , USABrookhaven National Laboratory, Upton, New York 11973, USA*
[2]*SUPA, School of Physics, The University of Edinburgh, Edinburgh EH9 3JZ, United Kingdom*
[3]*Physics Department, Columbia University, New York, New York 10027, USA*
[4]*School of Physics and Astronomy, University of Southampton, Southampton SO17 1BJ, United Kingdom*
[5]*Institute for Theoretical Physics, Kanazawa University, Kakuma, Kanazawa, 920-1192, Japan*
[6]*Institute of Particle and Nuclear Studies, KEK, Tsukuba, Ibaraki 305-0801, Japan*
[7]*Brookhaven National Laboratory, Upton, New York 11973, USA*
[8]*SUPA, Department of Physics & Astronomy, University of Glasgow, Glasgow G12 8QQ, United Kingdom*
(Received 3 January 2008; published 24 September 2008)

We present a calculation of the renormalization coefficients of the quark bilinear operators and the $K - \bar{K}$ mixing parameter B_K. The coefficients relating the bare lattice operators to those in the RI/MOM scheme are computed nonperturbatively and then matched perturbatively to the $\overline{\mathrm{MS}}$ scheme. The coefficients are calculated on the RBC/UKQCD $2 + 1$ flavor dynamical lattice configurations. Specifically we use a $16^3 \times 32$ lattice volume, the Iwasaki gauge action at $\beta = 2.13$ and domain wall fermions with $L_s = 16$.

DOI: 10.1103/PhysRevD.78.054510 PACS numbers: 11.15.Ha, 11.30.Rd, 12.38.−t, 12.38.Gc

I. INTRODUCTION

The RBC and UKQCD collaborations have recently performed the first simulations with $2 + 1$ flavor domain wall fermions [1–3]. Much interesting phenomenology requires the conversion of bare lattice quantities to a less arbitrary and more perturbatively amenable continuum scheme. In particular, this is true for the determination of weak matrix elements such as B_K and for the standard model parameters such as quark masses. Of course, physical quantities are independent of the choice of renormalization procedure, nevertheless theoretical predictions are often given in terms of the parameters of the theory (α_s and quark masses) which require renormalization. In addition, for many processes (e.g. $K - \bar{K}$ mixing) the amplitudes are factorized into products of perturbative Wilson coefficient functions and operator matrix elements which contain the long-distance effects. The Wilson coefficients and operator matrix elements need to be combined with both evaluated in the same renormalization scheme. The purpose of this paper is to determine the factors by which matrix elements computed in our numerical simulations should be multiplied in order to obtain those in the $\overline{\mathrm{MS}}$ scheme which is conventionally used for the evaluation of the coefficient functions.

In principle, for a sufficiently small lattice spacing a and a sufficiently large renormalization scale μ, it is possible to perform the renormalization of the bare lattice operators using perturbation theory. However, in practice the coefficients of lattice perturbation theory are frequently large leading to a poor convergence of the series and even with attempts such as *tadpole improvement* to resum some of the large contributions, it appears that the typical n-loop correction is numerically of $O(\alpha_s^n)$, in contrast to continuum perturbation theory where the corresponding contributions are of $O((\alpha_s/4\pi)^n)$. A related difficulty is the choice of the best expansion parameter (α_s), for example, between some tadpole improved lattice coupling or the $\overline{\mathrm{MS}}$ coupling. In practice, at one-loop order, different reasonable choices can lead to significantly different results. For the quark bilinear operators and B_K considered in this paper, we present the perturbative results and illustrate these points in Sec. II.

The main purpose of this paper is to avoid the uncertainties present when using lattice perturbation theory by implementing the Rome-Southampton RI/MOM nonperturbative renormalization technique [4]. The key idea of this technique is to define a sufficiently simple renormalization condition such that it can be easily imposed on correlation functions in any lattice formulation of QCD, or indeed in any regularization—that is, the condition is regularization invariant (RI). We therefore introduce counter-terms for any regularization such that a Landau gauge renormalized n-point correlation function with standard MOM kinematics at some scale μ^2 has its tree level value. This condition is simple to impose whenever the renormalized correlation function is known in any regularization. It applies equally well to both perturbative expansions to any order and to nonperturbative schemes such

*Current affiliation: Department of Physics, University of Virginia, Charlottesville, VA, USA.

as the lattice, and thus RI/MOM is a very useful interface for changing schemes. In particular, only continuum perturbation theory and the lattice regularization are required to obtain physical results from a lattice calculation.

Our choice of lattice action is important for the efficacy of the RI/MOM technique. With domain wall fermions, $O(a)$ errors and chiral symmetry violation can be made arbitrarily small at fixed lattice spacing by increasing the size of the fifth dimension. This allows us to avoid the mixing between operators which transform under different representations of the chiral symmetry group; this is a very significant simplification compared to some other formulations of lattice QCD. The action and operators are also automatically $O(a)$ improved.

Another important property of DWF is the existence of (nonlocal) conserved vector and axial currents. This will be discussed in detail below.

In this paper we study the renormalization of the quark bilinear operators $\bar{\psi}\Gamma\psi$, where Γ is one of the 16 Dirac matrices, and of the $\Delta S = 2$ four-quark operator O_{LL}. Table I contains a summary of our results, relating bare operators in the lattice theory with domain wall fermions and the Iwasaki gauge action at $\beta = 2.13$ ($a^{-1} = 1.729(28)$ GeV, see Sec. III for further details) to those in two continuum renormalization schemes. Columns three through five give the three independent Z-factors which, when multiplying the appropriate bilinear lattice operator, convert that operator into one normalized according to either the RI/MOM or $\overline{\text{MS}}$ (NDR) schemes. The final column contains the combination of factors needed to convert a lattice result for the parameter B_K into the corresponding RI/MOM or $\overline{\text{MS}}$ (NDR) value.

The plan of the remainder of the paper is as follows. In the following section (Sec. II) we start by reviewing the perturbative evaluation of the renormalization constants; the results can later be compared with those obtained using the nonperturbative procedures. In Sec. III, we begin the description of the nonperturbative computations with a brief introduction to the details of our simulation and to the computation of the quark propagators which are the basic building blocks for all our subsequent calculations. In Sec. IV we give a short introduction to the regularization independent (RI/MOM) scheme. In this section we also discuss the renormalization of flavor nonsinglet bilinear operators, including the check of the Ward-Takahashi identities. The discussion of the renormalization of the four-quark operators and the results for the renormalization constant for B_K are presented in Sec. V. Section VI contains a brief summary and our conclusions.

II. PERTURBATION THEORY

Before proceeding to describe our nonperturbative evaluation of the renormalization constants we briefly review the corresponding (mean field improved) perturbative calculations. Specifically, we present perturbative estimates for the renormalization constants of the quark bilinears and B_K. These can then be compared to those obtained nonperturbatively below. The ingredients for the perturbative calculations and a detailed description of the procedure can be found in Refs. [6,7].

Writing the domain wall height as $M = 1 - \omega_0$, the bare value of ω_0 in our simulation is $\omega_0 = -0.8$. The mean field improved value of ω_0 is then given by

$$\omega_0^{\text{MF}} = \omega_0 + 4(1 - u) \simeq -0.303, \tag{1}$$

where the link variable is defined by $u = \mathcal{P}^{1/4}$ and $\mathcal{P} = 0.588\,130\,692$ is the value of the plaquette in the chiral limit.

We define the renormalization constant, Z_{O_i}, which relates the bare lattice operator, $O_i^{\text{Latt}}(a^{-1})$, to the corresponding renormalized one in the $\overline{\text{MS}}$ scheme at a renormalization scale of $\mu = a^{-1}$ by:

$$O_i^{\overline{\text{MS}}}(a^{-1}) = Z_i O_i^{\text{Latt}}(a^{-1}). \tag{2}$$

Here $i = S, P, V, A, T$ for the scalar and pseudoscalar densities, vector and axial-vector currents, and tensor bilinear and $i = B_K$ for the $\Delta S = 2$ operator which enters into the K^0-$\bar{K}^0$ mixing amplitude (or more precisely for the ratio of the $\Delta S = 2$ operator and the square of the local axial current, which is the relevant combination for the determination of B_K). The one-loop, mean field improved estimates for the Z_i are:

$$Z_{S,P} = \frac{u}{1 - (\omega_0^{\text{MF}})^2} \frac{1}{Z_\omega^{\text{MF}}} \left(1 - \frac{\alpha_s C_F}{4\pi} 5.455\right) \tag{3}$$

$$Z_{V,A} = \frac{u}{1 - (\omega_0^{\text{MF}})^2} \frac{1}{Z_\omega^{\text{MF}}} \left(1 - \frac{\alpha_s C_F}{4\pi} 4.660\right) \tag{4}$$

TABLE I. The four factors $Z_{S,P}$, $Z_{V,A}$, Z_T and Z_{B_K} by which the matrix elements of the bare lattice bilinear operators and the ratio of matrix elements B_K should be multiplied in order to obtain the corresponding quantities renormalized in the RI/MOM or $\overline{\text{MS}}$(NDR) schemes. The RI/MOM quantities are defined at a scale $\mu = 2.037$ GeV, an available lattice momentum. The $\overline{\text{MS}}$(NDR) quantities are provided at the scale $\mu = 2$ GeV. The first error given is statistical and the second systematic. This table summarizes the main results of this paper. Note, the values shown for $Z_{V,A}$ are taken from Ref. [5].

Scheme	Scale	Z_q	$Z_{S,P}$	$Z_{V,A}$	Z_T	Z_{B_K}
RI/MOM	2.037 GeV	0.8086(28)(74)	0.466(14)(31)	0.7161(1)	0.8037(22)(55)	0.9121(38)(129)
$\overline{\text{MS}}$(NDR)	2.00 GeV	0.7726(30)(83)	0.604(18)(55)	0.7161(1)	0.7950(34)(150)	0.9276(52)(220)

$$Z_T = \frac{u}{1-(\omega_0^{\rm MF})^2}\frac{1}{Z_\omega^{\rm MF}}\left(1-\frac{\alpha_s C_F}{4\pi}3.062\right) \quad (5)$$

$$Z_{B_K} = 1-\frac{\alpha_s}{4\pi}1.470, \quad (6)$$

where C_F is the second Casimir invariant $C_F = (N^2-1)/2N$ for the gauge group $SU(N)$. Here $\sqrt{Z_w}$ is the quantum correction to the normalization factor $\sqrt{1-\omega_0^2}$ of the physical quark fields (the factors depending on this normalization cancel in the evaluation of Z_{B_K}). At one-loop order in perturbation theory

$$Z_w = 1+\frac{\alpha_s C_F}{4\pi}5.251. \quad (7)$$

In obtaining the coefficients in Eqs. (3)–(7) we have interpolated linearly between the entries for $M = 1.30$ and $M = 1.40$ in tables III and IV of Ref. [6] to the mean-field value of $M = 1.303$. Since the mean-field value of M is so close to the quoted values at $M = 1.30$, we prefer this procedure to using the general interpolation formula quoted in [6]. The difference between the two procedures is negligible compared to the remaining systematic uncertainties.

In order to estimate the numerical values of the renormalization constants we have to make a choice for the expansion parameter, i.e. the coupling constant α_s. Here we consider two of the possible choices, the mean-field value as defined in Eq. (62) of Ref. [7] and the $\overline{\rm MS}$ coupling, both defined at $\mu = a^{-1}$. The mean field improved coupling constant is given by

$$\frac{1}{g^2_{\rm MF}(a^{-1})} = \frac{\mathcal{P}}{g_0^2} + d_g + c_p + N_f d_f, \quad (8)$$

where g_0 is the bare lattice coupling constant ($g_0^2 = 6/\beta$), and the remaining parameters are defined in Ref. [7] and take the numerical values $d_g = 0.1053$, $c_p = 0.1401$ and for $\omega_0^{\rm MF} = -0.303$, $d_f = -0.001\,48$. We therefore obtain

$$\alpha_{\rm MF}(1.729\ {\rm GeV}) = 0.1769. \quad (9)$$

Such a value of the coupling is significantly lower than that in the $\overline{\rm MS}$ scheme at the same scale, for which we take, $\alpha^{\overline{\rm MS}}(1.729\ {\rm GeV}) = 0.3138$.

The difference in the two values of the coupling constant leads to a significant uncertainty in the estimates of the renormalization constants at this order, as can be seen in Table II. The need to eliminate this large uncertainty is the principle motivation for the use of nonperturbative renormalization. The entries in Table II are the factors by which the matrix elements of the bare lattice operators should be multiplied in order to obtain those in the $\overline{\rm MS}$(NDR) scheme at the renormalization scale $\mu = 1.729$ GeV.

Finally, we perform the renormalization group running from $\mu = 1.729$ GeV to obtain the normalization constants at other scales, and, in particular, at the conventional reference scale of $\mu = 2$ GeV (see Table III). In each case we use the highest order available for the anomalous dimension: two loops for B_K, three loops for the tensor operator, and four loops for the scalar/pseudoscalar densities. Whenever required, the strong coupling $\alpha_s(\mu)$ is evaluated using the four-loop beta function. However, when the beta function is needed to solve the renormalization group equations, we use only those terms up to the same order as is available for the corresponding anomalous dimension. This is the same procedure which we use for the nonperturbatively determined renormalization constants below and the details and references to the anomalous dimensions are presented in Secs. IV F, IV G, IV H, and V D below. The numbers in Table III are the factors by which the matrix elements of the bare lattice operators should be multiplied in order to obtain those in the $\overline{\rm MS}$(NDR) scheme at $\mu = 2$ GeV. The entries in the first

TABLE II. The factors, computed in perturbation theory, by which the matrix elements of the bare lattice operators should be multiplied in order to obtain those in the $\overline{\rm MS}$(NDR) scheme at the renormalization scale $\mu = 1.729$ GeV. This table shows that the difference in the choice of the strong coupling constant leads to large uncertainty in the renormalization constants.

Coupling	$Z_{S,P}(1.729\ {\rm GeV})$	$Z_{V,A}(1.729\ {\rm GeV})$	$Z_T(1.729\ {\rm GeV})$	$Z_{B_K}(1.729\ {\rm GeV})$
$\alpha_{\rm MF}(1.729\ {\rm GeV})$	0.788	0.801	0.827	0.979
$\alpha^{\overline{\rm MS}}(1.729\ {\rm GeV})$	0.672	0.693	0.737	0.963

TABLE III. The perturbative renormalization constants at the conventional scale of $\mu = 2$ GeV by renormalization group running from $\mu = 1.729$ GeV. The entries in the first column indicate which coupling was used in matching between the bare lattice operators and the $\overline{\rm MS}$ (NDR) scheme at $\mu = 1.729$ GeV.

Coupling	$Z_{S,P}(2\ {\rm GeV})$	$Z_{V,A}(2\ {\rm GeV})$	$Z_T(2\ {\rm GeV})$	$Z_{B_K}(2\ {\rm GeV})$
$\alpha_{\rm MF}(1.729\ {\rm GeV})$	0.822	0.801	0.813	0.993
$\alpha^{\overline{\rm MS}}(1.729\ {\rm GeV})$	0.701	0.693	0.725	0.977

column indicate which coupling was used in matching between the bare lattice operators and the $\overline{\text{MS}}$(NDR) scheme at $\mu = 1.729$ GeV, i.e. before the running to other scales.

III. SIMULATION DETAILS

The calculations described below were performed on the $2 + 1$ flavor dynamical lattice configurations generated by the RBC and UKQCD collaborations [2]. The lattices were generated with the Iwasaki gauge action at $\beta = 2.13$ and the domain-wall fermion action with $L_s = 16$. The size of the lattices used in this work is $16^3 \times 32$. The lattice spacing is $a^{-1} = 1.729(28)$ GeV and the residual mass $m_{\text{res}} = 0.003\,15(2)$ in lattice units [5]. We have 3 independent ensembles with light sea quark mass 0.01, 0.02, and 0.03, respectively. The strange sea quark mass is fixed at 0.04. For each ensemble, we have used 75 configurations, starting from trajectory number 1000 and with trajectory separation 40.

Following the Rome-Southampton RI/MOM nonperturbative renormalization procedure [4,8], the lattices are first fixed in Landau gauge. Then, on each gauge-fixed configuration, we measure the point-point quark propagators $S(x, x_0)$ with periodic boundary conditions in space and time, where x_0 is the source position and x is the sink. We have chosen four different sources to generate the propagators,

$$x_0 \in \{(0, 0, 0, 0), (4, 4, 4, 8), (7, 7, 7, 15), (12, 12, 12, 24)\}. \tag{10}$$

Next, a discrete Fourier transform is performed on the propagators,

$$S(p, x_0) = \sum_x S(x, x_0) \exp[-ip \cdot (x - x_0)], \tag{11}$$

where

$$p_\mu = \frac{2\pi}{L_\mu} n_\mu, \tag{12}$$

n_μ is a four-vector of integers and

$$L_x = L_y = L_z = 16 \qquad L_t = 32. \tag{13}$$

For the n_μ we take values in the ranges

$$\begin{aligned} n_x, n_y, n_z &\in \{-2, -1, 0, 1, 2\} \quad \text{and} \\ n_t &\in \{-4, -3, -2, -1, 0, 1, 2, 3, 4\} \end{aligned} \tag{14}$$

and require that the squared amplitude of the lattice momenta is in the range $0 \leq p^2 \lesssim 2.5$. In this paper, for simplicity of notation we frequently use lattice units for dimensionful quantities such as p and m. When we particularly wish to emphasize the nature of the discretization errors we explicitly reinstate the lattice spacing, writing, for example, $(ap)^2$ or $(am)^2$.

Our treatment of statistical errors follows the standard, single-elimination jackknife method. According to that method, we remove one of our 75 configurations and perform a complete calculation of the quantity of interest on the remaining 74 configurations. The average fluctuation among the results obtained by omitting, in turn, each of the 75 configurations is then multiplied by $\sqrt{75}$ to obtain the quoted statistical error. In order to check that possible correlations between our configurations have not led to an underestimate of the statistical error, we have repeated this procedure but removed first three and then five sequential configurations instead of one. The errors deduced from the resulting 25 and then 15 jackknife samples were equivalent to those obtained from the 75. In each case, we include the results from all four sources in a single bin so that possible correlations between the different sources will not lead to an underestimate of statistical errors. However, the results from the different sources appear to be very independent so that a reduction in statistical error of roughly a factor of 2 was achieved by this quadrupling of the computational effort.

IV. RENORMALIZATION OF QUARK BILINEARS

We now discuss how Green functions computed on the lattice can be used to obtain the nonperturbative renormalization constants relating bilinear operators defined on the lattice to those normalized first according to the RI/MOM and then the $\overline{\text{MS}}$ scheme. In the first two subsections below, Secs. IV A and IV B we briefly introduce the definitions and notation that we use in the rest of this paper. Some of these are extracted from the earlier RBC paper on quenched lattices [8] and are included here for completeness.

The definition of renormalization factors Z_q and Z_m for the quark wave function and mass in the RI/MOM scheme are given in Sec. IV A. The basic amputated quark-bilinear vertex functions are defined in Sec. IV B and the conditions defining the RI/MOM scheme are written down. Since our calculations are necessarily performed at finite momenta, the effects of chiral-symmetry breaking coming from both the nonzero quark masses and spontaneous chiral-symmetry breaking are visible. We discuss these effects in detail in Sec. IV C for the important case of the vector and axial-vector vertex functions.

Next, as a consistency check for our methods, we discuss the accuracy with which our off-shell vertex amplitudes satisfy the axial and vector Ward-Takahashi identities in Secs. IV D and IV E respectively. In the latter section, the determination of Z_S/Z_q is also discussed. In Sec. IV G we compare the observed scale dependence of Z_m with that predicted by perturbation theory and interpret the differences as coming from $(a\mu)^2$ errors. These are removed to determine first $Z_m^{\text{RI/MOM}}$ and then $Z_m^{\overline{\text{MS}}}$. A similar determination of $Z_q^{\text{RI/MOM}}$ and then $Z_q^{\overline{\text{MS}}}$ is presented in Sec. IV G.

Finally, in Sec. IV H, results for the tensor vertex renormalization factor Z_T are obtained.

A. Quark mass and wave function renormalization

First, we define the renormalization coefficients for the quark field and the quark mass as the ratio between the renormalized quantities and their bare counterparts,

$$q_{\rm ren}(x) = Z_q^{1/2} q_0(x) \tag{15}$$

$$m_{\rm ren} = Z_m m_0. \tag{16}$$

where $q_{\rm ren}$ and q_0 are the renormalized and the bare quark wave function, and $m_{\rm ren}$ and m_0 are the renormalized and the bare quark mass. With domain wall fermions,

$$m_0 = m_f + m_{\rm res} \tag{17}$$

where m_f is the input quark mass and $m_{\rm res}$ is the residual mass. The renormalized propagator (in momentum space) is

$$S_{\rm ren}(p, m_{\rm ren}) = Z_q S(p, m_0)|_{m_0 = m_{\rm ren}/Z_m} \tag{18}$$

where p is the momentum of the quark propagator.

Since domain wall quarks enter the calculations described here in three different ways we must be careful to clearly distinguish their three distinct masses. As described above, our calculations are performed with $2 + 1$ flavors of dynamical quarks. We will use the variable m_l to label the input mass m_f for the light dynamical quarks and m_s for that of the dynamical strange quark. Since we often evaluate products of propagators which depend on a third quark mass, that mass is labeled $m_{\rm val}$. In some cases the limit $m_{\rm val} \to 0$ may be an adequate definition of the chiral limit. However, in order to deal with simple results from which a weak quark mass dependence has been removed we will often consider the ''unitary'' case $m_{\rm val} = m_l$ and take the limit $m_{\rm val} = m_l \to 0$. Of course, in this case m_s remains nonzero but since its value is never changed this causes no immediate confusion. Underlying the validity of the Rome-Southampton renormalization scheme is the use of infrared-regular renormalization kinematics. Therefore, as our renormalization scale μ becomes larger and future calculations more accurate, even this weak quark mass dependence will completely disappear.

As discussed in detail in [8], the renormalization technique requires the existence of a window of momenta such that

$$\Lambda_{\rm QCD} \ll |p| \ll a^{-1}. \tag{19}$$

In practice, however, violation of these restrictions, especially at the higher boundary, has to be considered. Because of the spontaneous breaking of the chiral symmetry as illustrated by the nontrivial difference between Z_q/Z_A and Z_q/Z_V at low momenta (see Sec. IV C) we have to rely on the calculation in the relatively high momentum region, where $(ap)^2 \gtrsim 1$. Fortunately, the effects from breaking the restriction imposed by the finite lattice spacing a are small and predictable. They introduce an error of $\mathcal{O}((ap)^2)$ to the renormalization coefficients which can be removed by quadratic fitting to the momentum dependence. A more detailed investigation of this issue is presented in [8].

It is possible in principle to relax the constraint $|p| \gg \Lambda_{\rm QCD}$ in Eq. (19) by performing *step scaling*, i.e. by matching the renormalization conditions successively to finer (and also smaller in physical units) lattices. This is beyond the scope of this paper.

The regularization independent (RI/MOM) scheme is defined such that by adjusting the renormalization coefficients Z_q and Z_m at the renormalization scale μ, and restricting p in a suitable window, we have:

$$\lim_{m_{\rm ren}\to 0} -\frac{i}{12}\,{\rm Tr}\left(\frac{\partial S_{\rm ren}^{-1}}{\partial \not{p}}(p)\right)_{p^2=\mu^2} = 1 \tag{20}$$

$$\lim_{m_{\rm ren}\to 0} \frac{1}{12 m_{\rm ren}}\,{\rm Tr}(S_{\rm ren}^{-1}(p))_{p^2=\mu^2} = 1. \tag{21}$$

Imposing these conditions on the lattice and taking into account the dynamical breaking of chiral symmetry at low energies, the additive mass renormalization $m_{\rm res}$ and $\mathcal{O}(a^2)$ lattice artifacts, we have the following asymptotic behavior [8] for relatively large p^2:

$$\frac{1}{12}\,{\rm Tr}(S^{-1}(p)) = \frac{a^3\langle\bar{q}q\rangle}{(ap)^2} C_1 Z_q + Z_m Z_q\{am_{\rm val} + am_{\rm res}\} + \mathcal{O}((ap)^2). \tag{22}$$

The left-hand-side of Eq. (22) at each of the unitary points ($m_l = m_{\rm val}$) is calculated as the inverse of the average over all propagators, where the average is performed over all sources and configurations:

$$S(p)^{-1} = \left\{\frac{1}{N}\sum_{i=1}^{N}\left[\frac{1}{n_{\rm source}}\sum_{x_0} S_i(p, x_0)\right]\right\}^{-1} \tag{23}$$

where $n_{\rm source} = 4$ and $i \in \{1, 2, \cdots, N\}$ labels each configuration. Because of possible correlations between propagators with different sources calculated on the same configuration, each group of 4 propagators from the same configuration is considered as one jackknife bin in the single-elimination procedure.

In Fig. 1 we plot the results for $\frac{1}{12}\,{\rm Tr}[S^{-1}(p)]$ as a function of the momentum and tabulate the corresponding numerical values in Table IV. In addition to our results for nonzero quark mass, we also plot and tabulate the results extrapolated to the chiral limit where $m_l = m_{\rm val} = -m_{\rm res}$ for each momentum. Two quantities of interest can be deduced from the mass dependence shown in Fig. 1. First, the chiral limit gives a measure of the spontaneous and explicit chiral symmetry breaking and is given in the

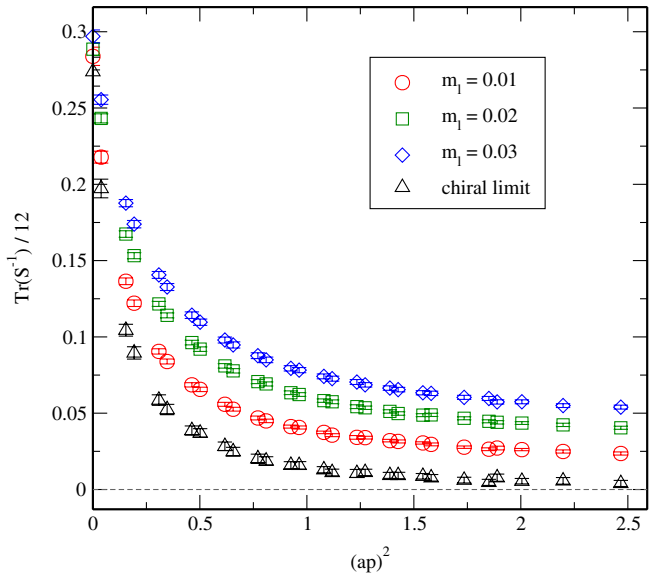

FIG. 1 (color online). The quantity $\frac{1}{12}\,\mathrm{Tr}(S^{-1})$ plotted versus $(ap)^2$ for the unitary mass points $m_l = 0.01$, 0.02, and 0.03 and at the linearly extrapolated, chiral limit $m_l = -m_{\mathrm{res}}$.

right-most column of Table IV. Second, determining the slope with respect to m_{val} provides one method to calculate $Z_m Z_q$. This is used later in Sec. IV E to test the vector Ward Identity which relates this to a second method of computing $Z_m Z_q$.

B. Renormalization of flavor nonsinglet fermion bilinears

We now consider the renormalization of quark bilinear operators of the form $\bar{u}\Gamma d$, where Γ is one of the 16 Dirac matrices. The corresponding renormalization constant Z_Γ is the factor relating the renormalized and bare bilinear operators:

$$[\bar{u}\Gamma d]_{\mathrm{ren}}(\mu) = Z_\Gamma(\mu a)[\bar{u}\Gamma d]_0, \tag{24}$$

where μ is the renormalization scale and we will treat only local operators where the lattice fields $\bar{u}$ and d in the bilinear operator $[\bar{u}\Gamma d]_0$ are evaluated at the same space-time point.

Following the Rome-Southampton prescription [4] for renormalization in the RI/MOM scheme, we define the bare Green functions between off-shell quark lines, and evaluate their momentum-space counterparts $G_{\Gamma,0}(p)$ on the lattice, averaged over all sources and gauge configurations,

$$G_{\Gamma,0}(p) = \frac{1}{N}\sum_{i=1}^{N}\left\{\frac{1}{n_{\mathrm{source}}}\sum_{x_0}[S_i(p,x_0)\Gamma(\gamma_5 S_i(p,x_0)^\dagger\gamma_5)]\right\}. \tag{25}$$

We then amputate this Green function using the averaged propagators,

$$\Pi_{\Gamma,0}(p) = S^{-1}(p)G_{\Gamma,0}(p)(\gamma_5[S^{-1}(p)]^\dagger\gamma_5), \tag{26}$$

where $S^{-1}(p)$ is calculated according to Eq. (23). The bare vertex amplitudes are obtained from the amputated Green functions as follows [4,8]:

$$\Lambda_S(p) = \tfrac{1}{12}\mathrm{Tr}[\Pi_1(p)1] \tag{27}$$

$$\Lambda_P(p) = \tfrac{1}{12}\mathrm{Tr}[\Pi_{\gamma_5}(p)\gamma_5] \tag{28}$$

$$\Lambda_V(p) = \frac{1}{48}\,\mathrm{Tr}\left[\sum_\mu \Pi_{\gamma_\mu}(p)\gamma_\mu\right] \tag{29}$$

$$\Lambda_A(p) = \frac{1}{48}\,\mathrm{Tr}\left[\sum_\mu \Pi_{\gamma_\mu\gamma_5}(p)\gamma_5\gamma_\mu\right] \tag{30}$$

$$\Lambda_T(p) = \frac{1}{72}\,\mathrm{Tr}\left[\sum_{\mu,\nu} \Pi_{\sigma_{\mu\nu}}(p)\sigma_{\nu\mu}\right]. \tag{31}$$

The values of all the five bare vertex amplitudes at the unitary mass points $m_l = m_{\mathrm{val}}$ are presented in Tables V, VI, and VII. Finally, by requiring that the renormalized vertex amplitudes satisfy

TABLE IV. The quantity $\frac{1}{12}\,\mathrm{Tr}(S^{-1})$ evaluated at the unitary mass points, $m_{\mathrm{val}} = m_l$ and linearly extrapolated to the chiral limit $m_l = -m_{\mathrm{res}}$.

$(ap)^2$	$m_l = 0.01$	$m_l = 0.02$	$m_l = 0.03$	chiral limit
0.347	0.0839(16)	0.1141(16)	0.1327(23)	0.0524(34)
0.617	0.0558(13)	0.0810(15)	0.0980(20)	0.0283(28)
0.810	0.0450(12)	0.0692(14)	0.0849(18)	0.0187(28)
1.079	0.03744(82)	0.0583(11)	0.0741(16)	0.0130(20)
1.234	0.0342(12)	0.0543(13)	0.0704(16)	0.0105(26)
1.388	0.03203(84)	0.0512(11)	0.0665(15)	0.0092(20)
1.542	0.03051(75)	0.04873(97)	0.0634(14)	0.0087(18)
1.851	0.02640(92)	0.04472(99)	0.0597(13)	0.0047(20)
2.005	0.02615(73)	0.04354(92)	0.0575(13)	0.0054(18)
2.467	0.0236(10)	0.0404(10)	0.0540(13)	0.0040(20)

TABLE V. The five bare vertex amplitudes Λ_i, $i \in \{S, P, V, A, T\}$ averaged over four sources, with $m_l = m_{\text{val}} = 0.01$.

$(ap)^2$	Λ_S	Λ_P	Λ_V	Λ_A	Λ_T
0.347	2.125(86)	6.72(19)	1.1702(58)	1.0675(43)	0.8904(43)
0.617	1.945(51)	4.45(11)	1.1419(37)	1.0938(30)	0.9404(26)
0.810	1.856(37)	3.677(81)	1.1348(31)	1.1025(27)	0.9618(19)
1.079	1.758(27)	3.022(57)	1.1335(29)	1.1135(27)	0.9882(16)
1.234	1.715(24)	2.792(50)	1.1291(29)	1.1137(27)	0.9935(17)
1.388	1.677(21)	2.600(43)	1.1328(26)	1.1191(24)	1.0065(13)
1.542	1.642(19)	2.448(38)	1.1355(27)	1.1240(25)	1.0167(14)
1.851	1.599(16)	2.239(32)	1.1387(29)	1.1301(27)	1.0310(16)
2.005	1.578(15)	2.154(28)	1.1420(27)	1.1342(26)	1.0392(16)
2.467	1.532(13)	1.979(23)	1.1495(29)	1.1434(29)	1.0577(19)

TABLE VI. The five bare vertex amplitudes Λ_i, $i \in \{S, P, V, A, T\}$ averaged over four sources, with $m_l = m_{\text{val}} = 0.02$.

$(ap)^2$	Λ_S	Λ_P	Λ_V	Λ_A	Λ_T
0.347	1.828(45)	5.09(14)	1.1745(46)	1.0412(28)	0.8930(31)
0.617	1.774(30)	3.600(82)	1.1465(30)	1.0838(21)	0.9414(18)
0.810	1.721(24)	3.052(61)	1.1360(24)	1.0943(19)	0.9614(15)
1.079	1.655(19)	2.590(45)	1.1331(22)	1.1069(20)	0.9870(12)
1.234	1.637(16)	2.428(40)	1.1307(21)	1.1083(20)	0.9930(12)
1.388	1.608(15)	2.283(33)	1.1323(21)	1.1141(19)	1.0049(11)
1.542	1.581(14)	2.175(30)	1.1351(21)	1.1199(20)	1.0159(12)
1.851	1.552(11)	2.019(24)	1.1389(22)	1.1275(21)	1.0309(12)
2.005	1.532(11)	1.955(23)	1.1416(23)	1.1315(22)	1.0390(14)
2.467	1.4984(91)	1.819(18)	1.1498(26)	1.1422(25)	1.0580(17)

TABLE VII. The five bare vertex amplitudes Λ_i, $i \in \{S, P, V, A, T\}$ averaged over four sources, with $m_l = m_{\text{val}} = 0.03$.

$(ap)^2$	Λ_S	Λ_P	Λ_V	Λ_A	Λ_T
0.347	1.723(56)	4.10(14)	1.1809(56)	1.0357(23)	0.9020(24)
0.617	1.702(37)	3.049(87)	1.1457(37)	1.0769(19)	0.9451(17)
0.810	1.663(28)	2.658(66)	1.1356(31)	1.0886(17)	0.9642(14)
1.079	1.610(21)	2.307(49)	1.1325(27)	1.1015(18)	0.9883(12)
1.234	1.591(18)	2.182(42)	1.1294(25)	1.1050(20)	0.9951(12)
1.388	1.569(15)	2.076(37)	1.1312(25)	1.1105(20)	1.0061(11)
1.542	1.548(13)	1.991(33)	1.1337(26)	1.1157(21)	1.0161(12)
1.851	1.520(10)	1.869(27)	1.1366(26)	1.1228(22)	1.0300(13)
2.005	1.5065(96)	1.820(25)	1.1395(27)	1.1271(24)	1.0382(15)
2.467	1.4764(78)	1.717(20)	1.1464(27)	1.1371(26)	1.0561(17)

$$\Lambda_{i,\text{ren}} = \frac{Z_i}{Z_q}\Lambda_i = 1, \qquad i \in \{S, P, V, A, T\}, \tag{32}$$

we can calculate the relevant renormalization constants.

Equations (24) through Eq. (32) describe the schematic procedure used to calculate the renormalization coefficients of quark bilinears. In practice however, with finite quark masses and a limited range of momenta, we have to consider lattice artefacts and other systematic uncertainties. We explain the details in the following sections.

C. Chiral symmetry breaking and $Z_A - Z_V$

In this section we examine the effects of both the low-energy spontaneous chiral symmetry breaking present in QCD and our nonzero quark masses on the large-momentum, off-shell propagators which we are using to

impose nonperturbative renormalization conditions. A good quantity to study in order to understand these effects is the difference of the off-shell vector and axial-vector vertex functions.

1. Numerical results for $Z_A - Z_V$

In the limit of a small mass and a large momentum, we expect

$$Z_A = Z_V, \tag{33}$$

or equivalently,

$$\Lambda_A(p^2) = \Lambda_V(p^2) \tag{34}$$

for $p^2 \gg \Lambda^2_{\rm QCD}, m^2$.

However, with finite quark masses and at relatively low momenta Λ_V and Λ_A may receive different contributions of the form

$$\frac{m^2_{\rm val}}{p^2} \tag{35}$$

and

$$\frac{m_{\rm val}\langle\bar{q}q\rangle}{p^4}. \tag{36}$$

Here we are exploiting the $SU_L(3) \times SU_R(3)$ chiral symmetry of large L_s domain wall fermions which implies that a difference between Λ_V and Λ_A requires the mixing of (8, 1) and (1, 8) representations and hence involves a product of two quantities which transform as $(3, \bar{3})$ and $(\bar{3}, 3)$. This requires the two powers of $m_{\rm val}$ in Eq. (35) and the product $m_{\rm val}\langle\bar{q}q\rangle$ in Eq. (36). The extra factors of $1/p^2$ and $1/p^4$ come from naive dimensional analysis.

To determine how much chiral symmetry breaking is present in our calculation, we examine the relative difference between Λ_A and Λ_V. In Fig. 2 we plot the quantity $\frac{\Lambda_A-\Lambda_V}{(\Lambda_A+\Lambda_V)/2}$ as a function of momentum. At relative low momenta, $0.5 \leq (pa)^2 \leq 1$, we observe that this quantity is quite large ($\sim$5%). Furthermore, even when we extrapolate $\frac{\Lambda_A-\Lambda_V}{(\Lambda_A+\Lambda_V)/2}$ to the chiral limit, where the terms in Eqs. (35) and (36) both vanish, the difference between Λ_A and Λ_V does not vanish. Here to obtain the chiral limit shown in Fig. 2 we perform a linear extrapolation $m_{\rm val} + m_{\rm res} \to 0$. While a quadratic extrapolation gives a similar result, this linear choice is motivated by the analysis presented in Sec. IV C 3.

Since the explicit chiral symmetry breaking effects needed to split Λ_A and Λ_V can be argued [9] to be $O(m^2_{\rm res})$, we would not expect this difference to reflect explicit, finite-L_s, domain wall chiral symmetry breaking. In fact, similar deviations between Λ_V and Λ_A are seen on lattice ensembles without fermion loops where explicit domain wall chiral symmetry breaking is expected to be smaller. This is shown in Fig. 3 where we plot the same quantities from a quenched simulation using the DBW2 gauge action. Thus, it appears that this difference represents the high energy tail of QCD dynamical chiral sym-

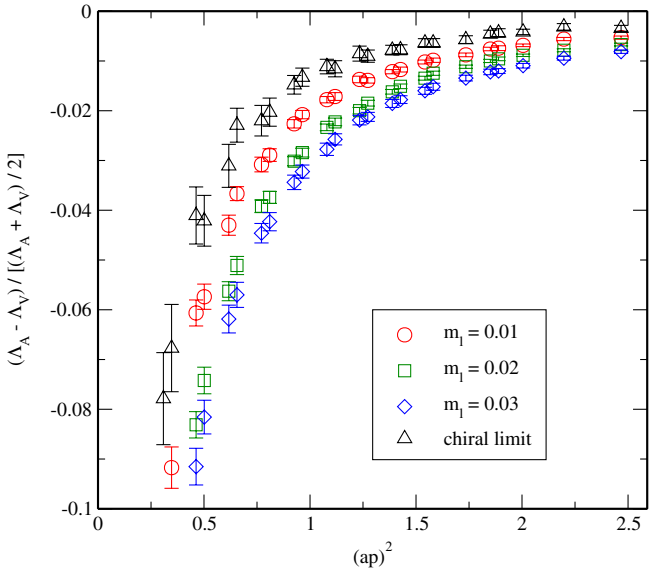

FIG. 2 (color online). The ratio $\frac{\Lambda_A-\Lambda_V}{(\Lambda_A+\Lambda_V)/2}$ plotted as a function of momentum at the unitary mass points $m_{\rm val} = m_l$ and in the chiral limit evaluated by linear extrapolation in m_l. The 5%–10% difference at low momentum decreases rapidly as the momentum increases. At the scale $\mu \simeq 2$ GeV, or $(ap)^2 \simeq 1.4$, the difference is about 1%, which contributes to the systematic error in Z_{B_K}.

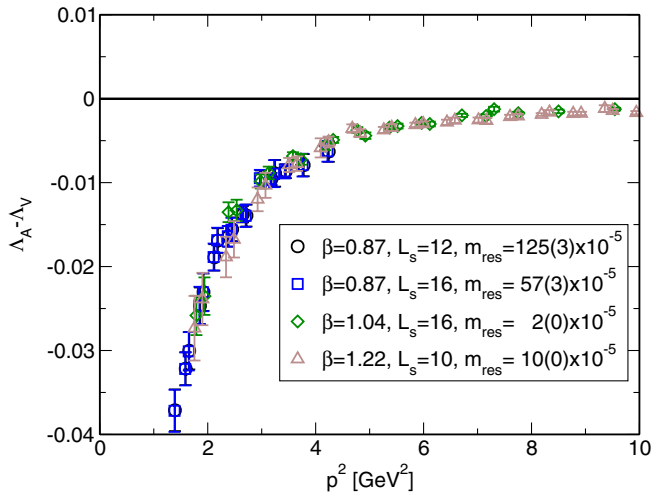

FIG. 3 (color online). The difference $\Lambda_A - \Lambda_V$ computed using four different quenched DBW2 lattice ensembles. These ensembles have quite different lattice scales. In addition the values of L_s, the extent in the 5th dimension used in computing the DWF propagators, also varies significantly. This provides compelling evidence that the observed chiral symmetry breaking is not an explicit breaking from finite L_s, but rather represents the high energy tail of QCD dynamical chiral symmetry breaking which would vanish if we were able to perform the NPR calculation at high enough energy. The data shown come from Refs. [16,28,29].

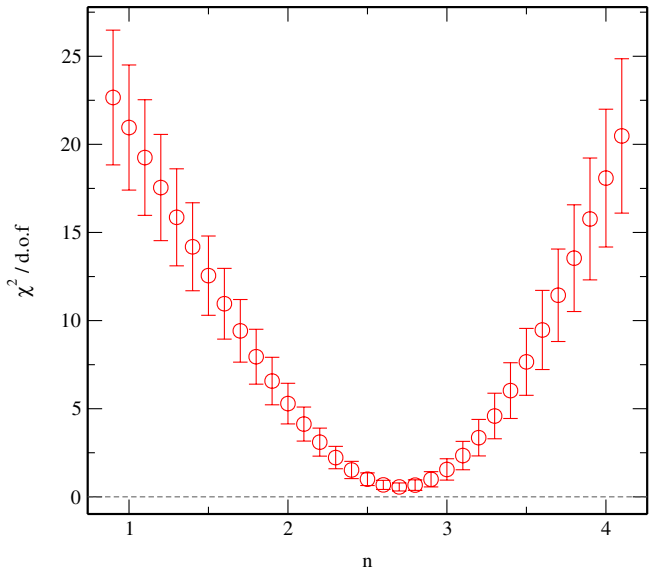

FIG. 4 (color online). The χ^2/d.o.f which results from fitting the momentum dependence of the quantity $\frac{\Lambda_A-\Lambda_V}{(\Lambda_A+\Lambda_V)/2}$ (extrapolated to the chiral limit) to the form p^{-n}. We conclude that the best choice for n lies between 2 and 3 and that it is unlikely that the term $\langle\bar{q}q\rangle^2/p^6$ gives the dominant contribution to this chiral symmetry breaking.

metry breaking rather than the explicit chiral symmetry breaking coming from the finite value of L_s.

While the effects of spontaneous chiral symmetry breaking will not vanish in the limit $m_{\rm val} + m_{\rm res} \to 0$, it is unlikely that the substantial difference found for $\Lambda_A - \Lambda_V$ in the chiral limit can be explained by a dimension-6 condensate such as

$$\frac{\langle\bar{q}q\rangle^2}{p^6} \tag{37}$$

since it is suppressed by six powers of momentum and appears to be too small for the size of the breaking we have observed. We have also fit the quantity $\frac{\Lambda_A-\Lambda_V}{(\Lambda_A+\Lambda_V)/2}$ to different powers of p, as is shown in Fig. 4, and it is clear that the momentum dependence of the chiral symmetry breaking term is dominated by p^{-2} or p^{-3}, very different from p^{-6} that naive dimensional analysis suggests should appear in the $\langle\bar{q}q\rangle^2$ term above.

2. Effects of exceptional momenta

In fact, we believe that the origin of the difference between Λ_A and Λ_V is different. Our choice of kinematics corresponds to so called "exceptional momenta," i.e. a momentum transfer is zero. This invalidates the naive power counting estimates used above and permits the low-energy, spontaneous chiral symmetry breaking to split Λ_V and Λ_A with only a $1/p^2$ suppression for large p, as we now explain. Begin by considering a general, amputated Feynman graph Γ with F external fermion lines and B external boson lines. Recall that for connected graphs the degree of divergence d of Γ is defined as $d = 4 - 3F/2 - B$. If the graph Γ is disconnected then its degree of divergence is the sum of those of its connected components. Now imagine that each external line of Γ carries an incoming momentum λp_i for $1 \le i \le F + B$, where λ is an overall scale factor. The asymptotic behavior for large λ of the amplitude corresponding to such a graph will be $\lambda^{d'}$ where d' is the degree of divergence of a subgraph $\Gamma' \subseteq \Gamma$. This subgraph Γ' must be chosen so that (i) there exists a routing of the internal momenta within Γ such that all lines carrying momenta proportional to λ lie within Γ' and (ii) Γ' possesses the least negative degree of divergence d' of all those subgraphs satisfying (i) [10,11]. Note, that Γ' may equal the original graph Γ and may itself be disconnected.

The most familiar situation is the case of nonexceptional momenta, defined as a momentum configuration in which no proper partial sum of the external momenta p_i vanishes. Under these circumstances all subgraphs Γ' obeying (i) must be connected. (Otherwise there would be zero momentum transfer between the groups of momenta entering each of the disconnected components.) This implies that the subgraph Γ' with the least negative degree of divergence is one with no additional external lines beyond those already appearing in Γ which in turn implies that this subgraph Γ' is the entire graph Γ. For the case of the vertex graph of interest, we deduce a constant behavior (up to logarithms) since $d = 4 - 1 - 2 \cdot 3/2 = 0$. (Here it is convenient to view this vertex graph as resulting from a normal Feynman graph in which an external vector boson is coupled to the vertex so the rules discussed above directly apply.)

This analysis not only gives the leading asymptotic behavior but also insures that extracting a few extra factors of the mass m or the chiral condensate $\langle\bar{q}q\rangle$ will make the degree of divergence of that graph more negative and hence make its asymptotic falloff more rapid, in the fashion suggested by naive power counting. For the case of interest, we would like to restrict a subset of the internal fermion lines of our graph Γ to carry only low momenta so that they will reflect the low-energy, spontaneous chiral symmetry breaking of QCD. By definition, these low momentum lines cannot enter the subgraph Γ' discussed above whose degree of divergence determines the asymptotic behavior of amplitude being studied and whose internal momenta must be unconstrained. In order to split Λ_V and Λ_A, chiral symmetry breaking transforming as an (8, 8) under $SU(3) \times SU(3)$ is required. This in turn requires that the excluded subgraph, containing these low-momentum lines, must be joined to the remainder of the graph by at least four fermion lines. Under these circumstances the subgraph Γ' can no longer be the entire graph. It must be a proper subgraph and will therefore have additional external lines, in addition to those of Γ. Consequently Γ' must have a more negative degree of divergence than that of Γ.

Such a circumstance is illustrated by the general vertex graph Γ in Fig. 5, contained in the outer dashed box. Here we have identified a subgraph Γ_2 which carries only low momenta and can therefore transform as (8, 8) even in the limit of vanishing quark mass, $m_{\rm val} + m_{\rm res} = 0$. For the case of nonexceptional momenta, we must apply Weinberg's theorem to the subgraph Γ', enclosed in the inner dashed box, through which, by assumption, all of the large momenta entering the vertex and the two external fermion lines must be routed. Because of its connections to the subgraph Γ_2, the subgraph Γ' has six external fermion lines and one external boson line (connected to the vertex). The resulting degree of divergence is $d' = 4 - 1 - 6 \cdot 3/2 = -6$, justifying the naive $1/p^6$ behavior in Eq. (37).

However, in our case Λ_V and Λ_A are being evaluated with zero momentum entering the current vertex and with a vanishing sum of the two incoming fermion momenta—a configuration of exceptional momentum. For such a choice of external momenta we can divide the subgraph Γ' identified above into two pieces Γ_1 and Γ_3. Because the momenta are exceptional with no large momenta entering the vertex, we can route all of the large momenta through Γ_3. Since Γ_3 has only four external fermion lines, its degree of divergence is $d_3 = 4 - 4 \cdot 3/2 = -2$ and the $1/p^6$ behavior above has been replaced by the much less suppressed $1/p^2$. If we think of the subgraph Γ_2 as a generalized chiral condensate $\langle 0|\bar{q}q\bar{q}q|0\rangle$ we are seeing the asymptotic behavior

$$\frac{\langle 0|\bar{q}q\bar{q}q|0\rangle}{p^2}, \tag{38}$$

very consistent with our numerical results. Note the discrepancy in dimensions between Eqs. (37) and (38) will be made up by four powers of $\Lambda_{\rm QCD}$, the momentum scale to which the subgraph Γ_2 is restricted.

A simple class of graph allowing this behavior can be seen in Fig. 6. Here the large momentum carried by the two external fermion lines can be routed through the gluon propagator that is shown explicitly so that the upper part of the diagram carries only low momenta. The large momentum behavior of the gluon propagator gives the expected $1/p^2$ behavior. The two general fermion propagators shown with the shaded "blobs" carry small momenta and, as suggested by Eq. (22), can show $(3, \bar{3})$ or $(\bar{3}, 3)$ chiral symmetry violation even when $m_{\rm val} + m_{\rm res} = 0$.

To confirm this analysis, we have also calculated the difference between Λ_A and Λ_V with nonexceptional momenta. We have chosen 5 different momentum scales, each corresponding to a set of momenta which satisfy the condition $p_1^2 = p_2^2 = (p_1 - p_2)^2 = p^2$ for five values of p^2, as listed in Tables VIII and IX. We then calculated Λ_A and Λ_V with the two external fermions carrying respectively p_1 and p_2. The result is plotted in Fig. 7, which shows that the chiral symmetry breaking vanishes almost completely with nonexceptional kinematics at medium to large momenta.

While it would be more satisfactory to perform the calculations presented in this paper using nonexceptional momenta, the resulting RI/MOM normalization conditions would not correspond to those for which perturbative matching calculations have been carried out. Thus, we would not be able to relate the quantities which we calcu-

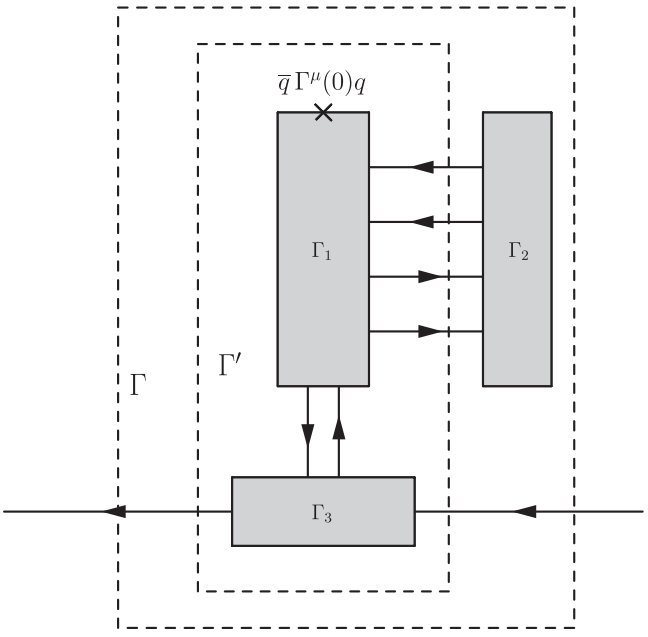

FIG. 5. The division of a general vertex graph into subgraphs. If the four-legged, internal subgraph Γ_2 carries momenta $p \sim \Lambda_{\rm QCD}$ it can introduce low energy, (8, 8) chiral symmetry breaking into such an amplitude even in the limit that the momenta external to the entire diagram Γ, included in the outer dashed box, grow large. As discussed in the text, such a limit will be suppressed by $1/p^6$ if the external momenta are nonexceptional but by only $1/p^2$ for the exceptional case.

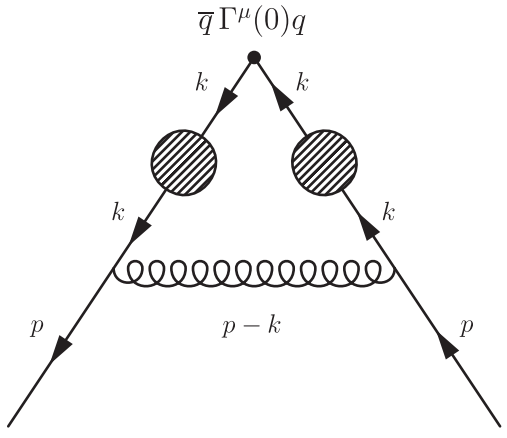

FIG. 6. Sample diagram in which two low-momentum ($k \simeq \Lambda_{\rm QCD}$) fermion propagators appear in a graph which is suppressed at high momentum only by a single factor of $1/p^2$.

TABLE VIII. Groups of nonexceptional momenta satisfying $p_1^2 = p_2^2 = (p_1 - p_2)^2$. The individual integers (n_x, n_y, n_z, n_t) should be multiplied by $2\pi/L_d$, with $L_x = L_y = L_z = 16$ and $L_t = 32$.

$(ap)^2$	p_1	p_2
0.617	(1, 1, 1, 2)	(1, −1, 1, 2)
	(1, 1, 1, 2)	(1, 1, −1, 2)
	(1, 1, 1, 2)	(−1, 1, 1, 2)
	(1, 1, 1, 2)	(1, 1, 1, −2)
	(1, 1, 1, 2)	(0, 0, 0, 4)
	(1, 1, 1, 2)	(0, 0, 2, 0)
	(1, 1, 1, 2)	(0, 2, 0, 0)
	(1, 1, 1, 2)	(2, 0, 0, 0)
0.925	(−1, −1, −2, 0)	(−2, −1, 0, −2)
	(−1, −1, −2, 0)	(−2, −1, 0, 2)
	(−1, −1, −2, 0)	(−2, 1, −1, 0)
	(−1, −1, −2, 0)	(−1, −2, 0, −2)
	(−1, −1, −2, 0)	(−1, −2, 0, 2)
	(−1, −1, −2, 0)	(−1, 0, −1, −4)
	(−1, −1, −2, 0)	(−1, 0, −1, 4)
	(−1, −1, −2, 0)	(0, −1, −1, −4)
	(−1, −1, −2, 0)	(0, −1, −1, 4)
	(−1, −1, −2, 0)	(0, 1, −2, −2)
	(−1, −1, −2, 0)	(0, 1, −2, 2)
	(−1, −1, −2, 0)	(1, −2, −1, 0)
	(−1, −1, −2, 0)	(1, 0, −2, −2)
	(−1, −1, −2, 0)	(1, 0, −2, 2)

TABLE IX. Groups of nonexceptional momenta satisfying $p_1^2 = p_2^2 = (p_1 - p_2)^2$, continuing Table VIII.

$(ap)^2$	p_1	p_2
1.234	(0, 2, 2, 0)	(2, 2, 0, 0)
	(0, 2, 2, 0)	(0, 2, 0, 4)
	(0, 2, 2, 0)	(0, 0, 2, 4)
	(0, 2, 2, 0)	(−2, 2, 0, 0)
	(0, 2, 2, 0)	(0, 2, 0, −4)
	(0, 2, 2, 0)	(2, 0, 2, 0)
	(0, 2, 2, 0)	(0, 0, 2, −4)
	(0, 2, 2, 0)	(−2, 0, 2, 0)
1.542	(1, 1, 2, 4)	(2, 1, 2, −2)
	(1, 1, 2, 4)	(1, −2, 2, 2)
	(1, 1, 2, 4)	(−2, 1, 2, 2)
	(1, 1, 2, 4)	(−2, 1, 1, 4)
	(1, 1, 2, 4)	(1, 2, 2, −2)
	(1, 1, 2, 4)	(1, −2, 1, 4)
	(1, 1, 2, 4)	(2, 1, −1, 4)
	(1, 1, 2, 4)	(1, 2, −1, 4)
2.467	(2, 2, 2, 4)	(2, 2, −2, 4)
	(2, 2, 2, 4)	(2, −2, 2, 4)
	(2, 2, 2, 4)	(−2, 2, 2, 4)
	(2, 2, 2, 4)	(2, 2, 2, −4)

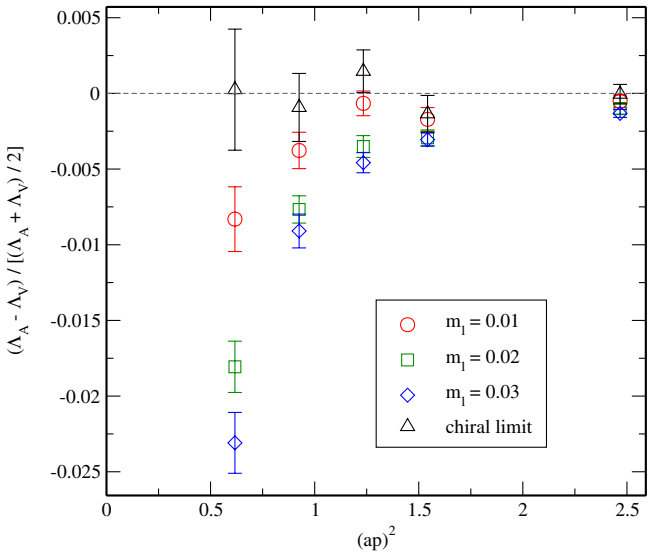

FIG. 7 (color online). The value of $\frac{\Lambda_A - \Lambda_V}{(\Lambda_A + \Lambda_V)/2}$ calculated with nonexceptional kinematics, which requires the sum of any subset of external momenta be nonzero. With this condition the chiral symmetry breaking is highly suppressed (as compared to Fig. 2) and vanishes almost completely over the available momentum region.

lated to those defined in the $\overline{\text{MS}}$ scheme. (Of course, this difficulty will be removed when the necessary perturbative calculations have been extended to nonexceptional kinematics.) A second, less significant advantage of the exceptional momenta which we use is that the exceptional momentum conditions are satisfied by a much larger set of discrete lattice momenta permitting the RI/MOM condition to be satisfied for more fine-grained sequence of energy scales.

We now return to the calculation with exceptional momenta ($p_1 = p_2$), at the scale which we are most interested in, that is $\mu \simeq 2$ GeV or $(ap)^2 \simeq 1.3$, where Λ_A and Λ_V have a difference of about 1%. Since we have no means to determine which of these two quantities has less contamination from low-energy chiral symmetry breaking we have decided to take the average $\frac{1}{2}(\Lambda_A + \Lambda_V)$ as the central value for both Z_q/Z_A and Z_q/Z_V. The difference between Λ_A or Λ_V and $\frac{1}{2}(\Lambda_A + \Lambda_V)$ then provides an estimate for one systematic error in our final results. The value of $\frac{1}{2}(\Lambda_A + \Lambda_V)$ is plotted in Fig. 8.

3. Chiral extrapolation to vanishing quark mass

As discussed above, our use of exceptional momenta implies a $1/p^2$ suppression for both terms behaving as m_{val} and m_{val}^2. The added dimension of a m_{val}^2 term can be provided by a factor of $1/\Lambda_{\text{QCD}}$ without the need to introduce additional inverse powers of p. For our largest value of $m_{\text{val}}a = 0.03$, we might estimate $m_{\text{val}}/\Lambda_{\text{QCD}} \approx 0.2$. This suggests that we should expect a linear rather than

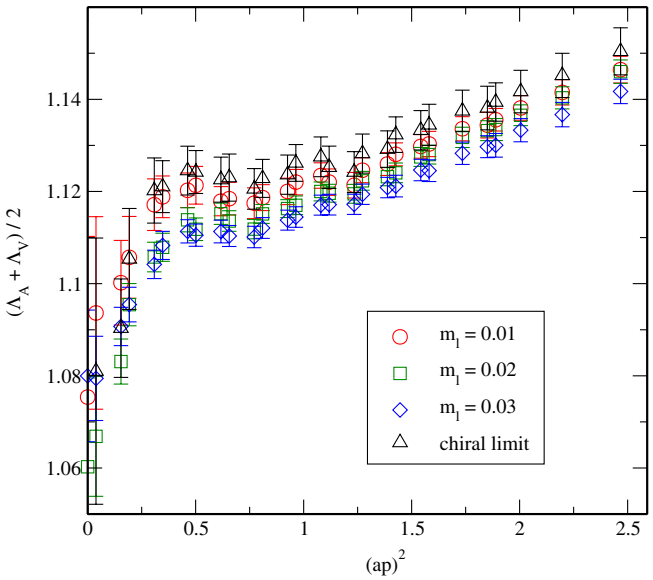

FIG. 8 (color online). The average $\frac{1}{2}(\Lambda_A + \Lambda_V)$ plotted as a function of momentum and evaluated for a unitary choice of masses and in the chiral limit. The chiral limit is taken using a linear fit.

quadratic behavior in m_{val} to dominate the small quark mass limit.

The difference $\Lambda_A - \Lambda_V$ discussed above provides a good place to study this effect. This difference reflects the chiral symmetry breaking of interest and may make these effects stand out with possibly reduced errors because of the statistical correlations between the two quantities being subtracted. Figure 9 compares linear and quadratic fits to the dependence on the quark mass evaluated at unitary points with $m_{\text{val}} = m_l + m_{\text{res}}$ for $p = 2.04$ GeV. In Table X we present the results of these two fits:

$$\frac{\Lambda_A - \Lambda_V}{(\Lambda_A + \Lambda_V)/2} = c_0 + c_1 \frac{m_{\text{val}} \Lambda_{\text{QCD}}}{p^2} \tag{39}$$

$$\frac{\Lambda_A - \Lambda_V}{(\Lambda_A + \Lambda_V)/2} = c_0 + c_2 \frac{m_{\text{val}}^2}{p^2}, \tag{40}$$

for $\Lambda_{\text{QCD}} = 319.5$ MeV. As can be seen in the table the linear fits are favored. The linear fits have the smaller χ^2 and the coefficient c_1 is significantly closer to an expected value of order 1 than is the coefficient c_2. Thus, based on both the theoretical expectation and this rough empirical evidence, we will adopt this linear description in the remainder of this paper and extrapolate our exceptional momentum amplitudes to the chiral limit using a linear ansatz. For the case at hand, Fig. 10 shows this linear extrapolation for the average $\frac{1}{2}(\Lambda_A + \Lambda_V)$ to the chiral limit for the momentum $p = 2$ GeV. Figure 8 shows the results in the chiral limit as a function of momentum. The results in the chiral limit are also presented in Table XI.

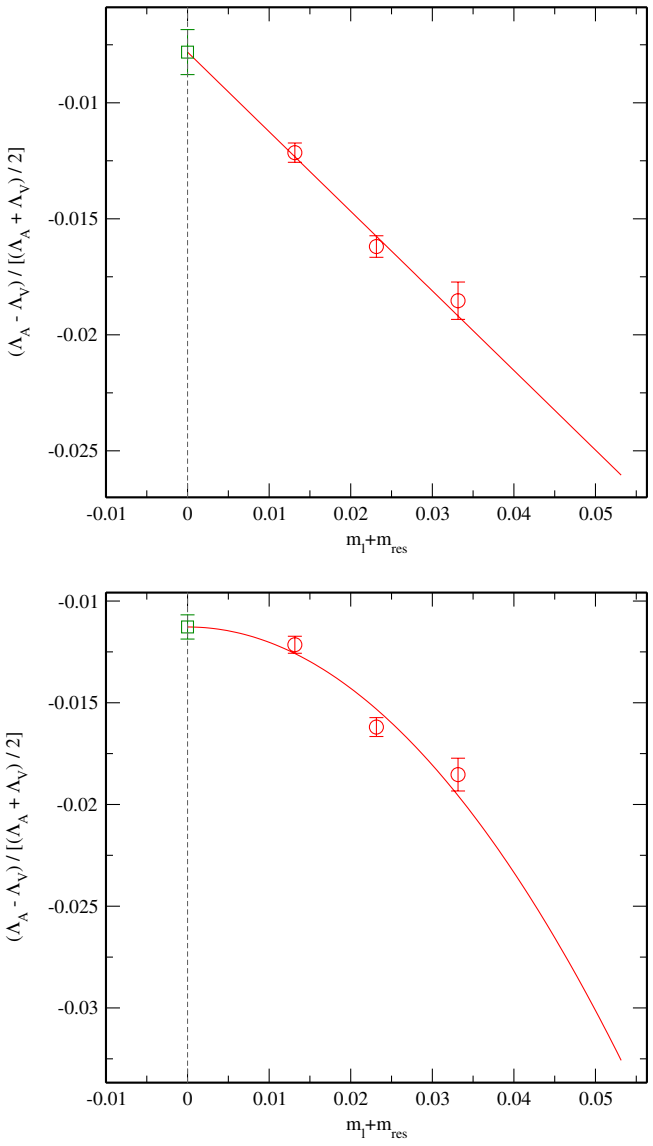

FIG. 9 (color online). Comparison of linear [Eq. (39)—top panel] and quadratic [Eq. (40)—bottom panel] fits to the dependence of the chiral symmetry breaking difference $\frac{(\Lambda_A - \Lambda_V)}{(\Lambda_A + \Lambda_V)/2}$ on the quark mass $m_{\text{val}} = m_l$ at the scale $\mu = 2.04$ GeV. These plots suggest that a linear description is more accurate. This conclusion is borne out by the properties of the actual fits shown in Table X.

D. Axial Ward-Takahashi identity

Performing an axial rotation on the propagator leads to a relation between Λ_P and $\text{Tr}(S^{-1})$, the axial Ward-Takahashi identity [8]:

$$\Lambda_P(p) = \frac{1}{12} \frac{\text{Tr}[S^{-1}(p)]}{(m_{\text{val}} + m_{\text{res}})}. \tag{41}$$

In a truly chiral theory or the present DWF calculation in the limit $L_s \to \infty$ (when chiral symmetry becomes exact and $m_{\text{res}} = 0$), this identity will be obeyed configuration by

TABLE X. Results from fitting the coefficient for mass term in $(\Lambda_A - \Lambda_V)/[(\Lambda_A + \Lambda_V)/2]$. The linear dependence is assumed to be $c_1 \frac{m\Lambda_{\rm QCD}}{p^2}$ and the quadratic dependence is assumed to be $c_2 \frac{m^2}{p^2}$. The respective χ^2/d.o.f is also listed. Both the coefficient c_1 more nearly agreeing with its expected value of 1 and the smaller χ^2 suggest that the linear description is to be preferred. We use the value $\Lambda_{\rm QCD} = 319.5$ MeV.

$(ap)^2$	c_1	$(\chi^2/\text{dof})_1$	c_2	$(\chi^2/\text{dof})_2$
0.347	−3.84(75)	3.0(3.4)	−14.7(3.1)	6.6(5.1)
0.617	−3.33(67)	2.2(2.8)	−12.9(2.8)	5.4(4.4)
0.810	−3.06(56)	1.2(2.1)	−12.1(2.5)	4.1(3.7)
1.079	−3.01(42)	0.4(1.3)	−12.4(2.0)	3.3(3.6)
1.234	−2.96(47)	6.2(5.0)	−11.4(2.1)	12.8(7.2)
1.388	−2.58(36)	1.7(2.7)	−10.5(1.7)	6.2(4.8)
1.542	−2.49(34)	0.4(1.4)	−10.2(1.6)	3.3(3.6)
1.851	−2.33(35)	0.06(41)	−9.5(1.6)	1.8(2.4)
2.005	−2.21(28)	0.02(23)	−9.2(1.3)	1.3(2.2)
2.467	−1.89(32)	0.01(22)	−7.4(1.4)	0.7(1.5)

configuration. However, for finite L_s and $m_{\rm res} \neq 0$, this relation will hold only after a gauge field average, (e.g. $m_{\rm res}$ is only defined after such an average). Thus, we should check Eq. (41) on gauge-averaged amplitudes.

Figure 11 shows the difference between the l.h.s and r.h.s of Eq. (41), divided by their average. The case of $m_l = 0.01$ shows a relatively larger breaking of $\leq 8\%$, while the other two masses result in a smaller breaking. For this smallest, 0.01 mass value, the $m_{\rm res}$ term (with a value of 0.003 08) is 30% of the $m_{\rm val} = 0.01$ term. This treatment of $m_{\rm res}$ as a simple constant will be accurate up to the corrections of higher order in the lattice spacing which appear in the equation defining $m_{\rm res}$. The largest such corrections should arise from the dimension-5, chromo-magnetic term, $\bar{q}\sigma^{\mu\nu}\gamma^5 F^{\mu\nu} q$, which also enters the divergence of the Furman-Shamir axial current [12]. The contributions of such a term are expected to be suppressed relative to those from $m_{\rm res}$ by only a factor $(pa)^2$ which is actually of order 1 for the kinematics shown in Fig. 11. Thus, we might expect to see violations in the region $(pa)^2 \approx 1$ of order $m_{\rm res}/0.01 \approx 30\%$. Fortunately the violations are considerably smaller but the expected rise with $(pa)^2$ may be visible. Of course, given the size of the errors shown in Fig. 11, the evidence for any violation of Eq. (41) is itself only 2 standard deviations.

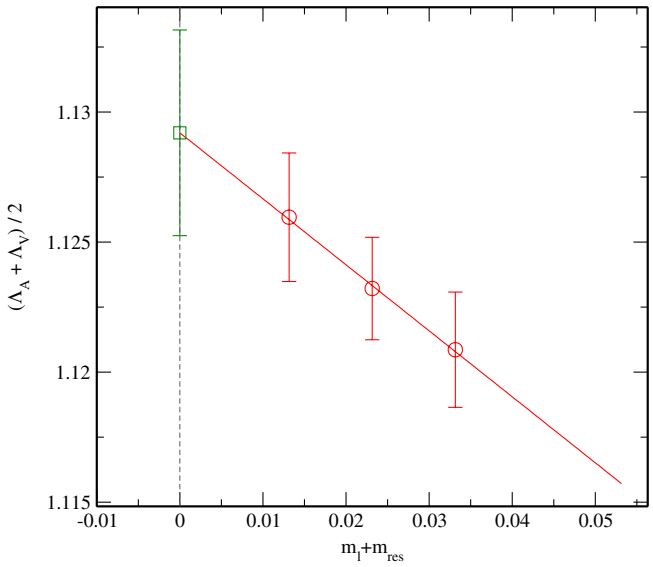

FIG. 10 (color online). A plot showing the linear extrapolation of $\frac{1}{2}(\Lambda_A + \Lambda_V)$ (evaluated at the scale $\mu = 2.04$ GeV) to the chiral limit. The three data points are evaluated at the unitary points $m_{\rm val} = m_l$.

E. Vector Ward-Takahashi identity and the chiral limit of Λ_S

Similar to the case with Λ_P, from the continuum vector Ward-Takahashi identity, we have the relation between Λ_S and $\text{Tr}(S^{-1})$ [8]:

$$\Lambda_S = \frac{1}{12} \frac{\partial \,\text{Tr}[S^{-1}(p)]}{\partial m_{\rm val}}. \tag{42}$$

TABLE XI. Values for $\frac{1}{2}(\Lambda_A + \Lambda_V)$, Λ_S, and Λ_T extrapolated to the chiral limit using a linear mass fit.

$(ap)^2$	$\frac{1}{2}(\Lambda_A + \Lambda_V)$	Λ_S	Λ_T
0.347	1.1211(56)	2.28(14)	0.8800(66)
0.617	1.1226(49)	2.060(88)	0.9363(36)
0.810	1.1228(41)	1.952(66)	0.9593(25)
1.079	1.1275(43)	1.836(47)	0.9873(22)
1.234	1.1242(44)	1.784(43)	0.9915(22)
1.388	1.1292(40)	1.736(37)	1.0061(18)
1.542	1.1333(43)	1.694(32)	1.0169(20)
1.851	1.1381(47)	1.644(27)	1.0319(24)
2.005	1.1417(46)	1.617(25)	1.0400(27)
2.467	1.1504(51)	1.564(22)	1.0593(33)

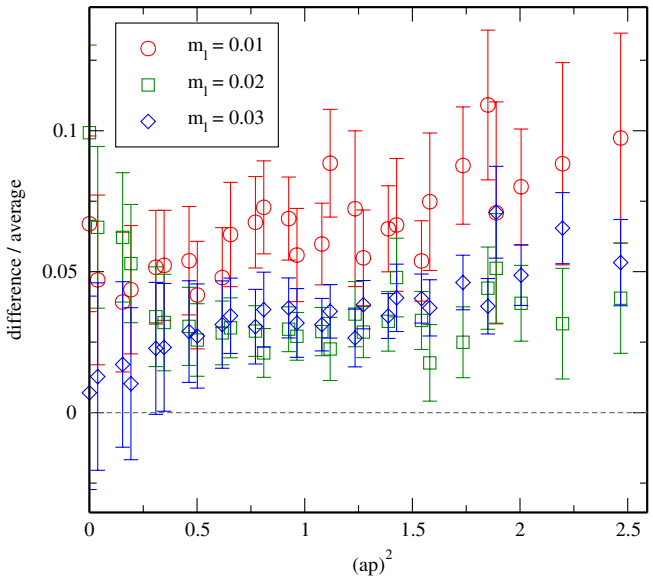

FIG. 11 (color online). The difference between the quantities Λ_P and $\frac{1}{12}\frac{\mathrm{Tr}(S^{-1})}{m_l+m_{\mathrm{res}}}$, divided by their average is plotted versus momentum for unitary quark masses. This provides a test of the axial Ward-Takahashi identity.

We are able to check our data against this identity using the three sources, (0, 0, 0, 0), (4, 4, 4, 8) and (12, 12, 12, 24) since it is only for these three sources that multiple valence mass data are available for each sea quark mass. We determine the derivative with respect to the valence quark mass on the right-hand-side of Eq. (42) from the slope of a linear fit of $\mathrm{Tr}[S^{-1}(p)]$ as a function of m_{val}.

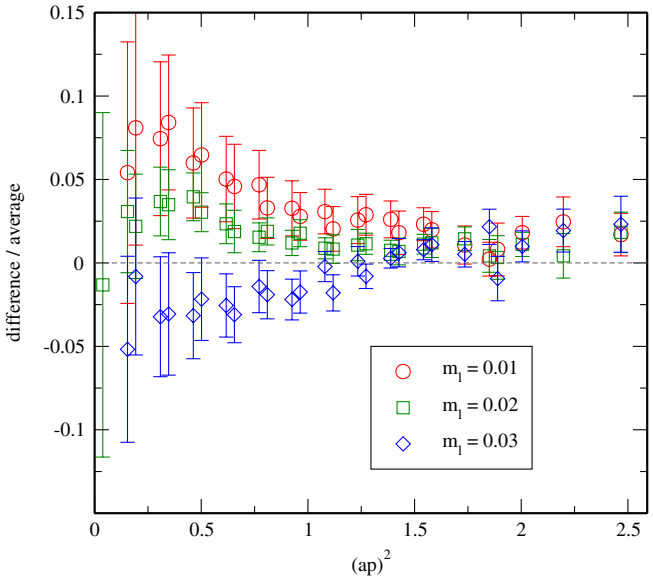

FIG. 12 (color online). The difference between the quantities Λ_S and $\frac{1}{12}\frac{\partial\,\mathrm{Tr}[S^{-1}(p)]}{\partial m_{\mathrm{val}}}$, divided by their average for each sea quark mass. The difference appears to zero within errors. This is a test of the vector Ward-Takahashi identity. The plot uses propagators from three sources.

Figure 12 shows the difference between the two sides of Eq. (42) divided by their average. For all three sea quark masses the data agrees well with the vector Ward-Takahashi identity [Eq. (42)] for medium to large momenta. Equation (42) implies the relation

$$Z_m = \frac{1}{Z_S}. \tag{43}$$

We will use this equation and a calculation of Λ_S to determine the mass renormalization factor in the following sections.

To extrapolate Λ_S to the chiral limit, we will improve upon the discussion in [8] in two regards. First, as explained above, we will exploit the asymptotic properties of Feynman amplitudes evaluated at exceptional momenta and assume that the leading mass dependence in the chiral limit will be linear in m. This is different from the m^2 dependence assumed in Ref. [8] where dimensional arguments, appropriate to the nonexceptional case and leading to the m^2 behavior in Eq. (35) were adopted.

Second, in contrast to that earlier quenched calculation we can examine the behavior of Z_S as a function of both the valence and light dynamical quark masses, m_{val} and m_l respectively. In Fig. 13 we plot Λ_S as a function of both m_{val} and m_l. The three curves are each a linear plus double pole fit to the valence quark mass dependence of the form:

$$\Lambda_S(m_{\mathrm{val}}, m_l) = c_0(m_l) + c_1(m_l)m_{\mathrm{val}} + c_{dp}\frac{m_l^2}{m_{\mathrm{val}}^2}, \tag{44}$$

where we have allowed the coefficients c_0 and c_1 of the constant and linear terms to vary with the dynamical light

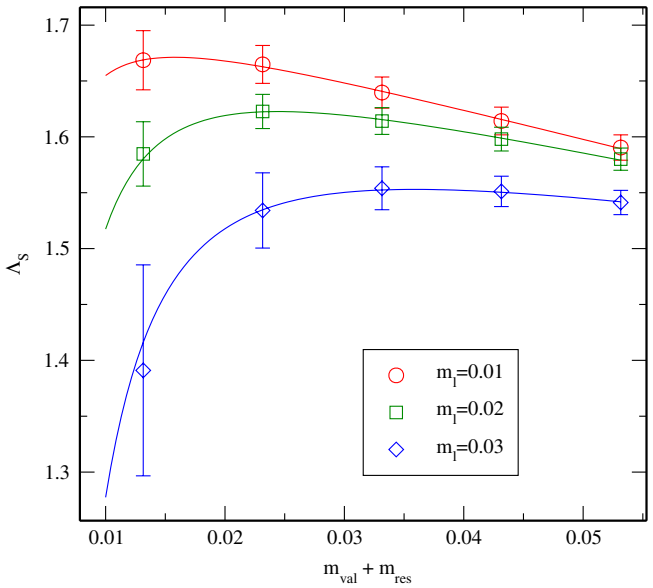

FIG. 13 (color online). The double-pole fit for Λ_S at $\mu = 2.04$ GeV. The expected decrease in the pronounced m_{val} dependence as the dynamical light quark mass m_l decreases is easily seen.

quark mass. However, we have used a common double-pole term with the m_l^2 behavior expected for a theory with two light flavors. Recall that this double pole term arises from topological near-zero modes [8] which for two light flavors will be suppressed by two powers of the light quark mass. The data in Fig. 13 shows just this behavior with the sharp turnover at the smallest value of $m_{\rm val}$ increasing as the light dynamical mass m_l increases.

This double-pole can be deduced from Eq. (42). As discussed in Ref. [8], the NLO, $1/p^2$ term derived from an operator product expansion of the quark propagator on the right-hand side of this equation is proportional to the chiral condensate $\langle \bar{q}q \rangle$ [13,14]. Isolated, topological, near-zero modes of the sort that arise from a gauge field background with nonzero Pontryagin index will contribute a term to the chiral condensate which behaves as $1/m_{\rm val}$. This implies that the derivative in Eq. (42) will yield the double pole, $1/m_{\rm val}^2$ hypothesized in Eq. (44). Such a near-zero mode will also introduce a factor of m_l into the fermion determinant of the QCD measure for each light flavor in the theory, hence the expected factor of m_l^2 in the numerator of Eq. (44). In Fig. 14 we show the variation of the double pole coefficient with the momentum at which the coefficient of the double pole was extracted. Also shown in this figure is a fit to the expected $1/p^2$ behavior which describes the results very well.

This understanding of the double pole terms suggests that a good strategy for extracting the chiral limit of Λ_S first takes the limit of vanishing m_l to remove this NLO double pole term and then extrapolates to $m_{\rm val} = 0$. In the present case, we perform the simpler linear fit using the unitary points to obtain $\Lambda_S = Z_q/Z_S$ since we do not have

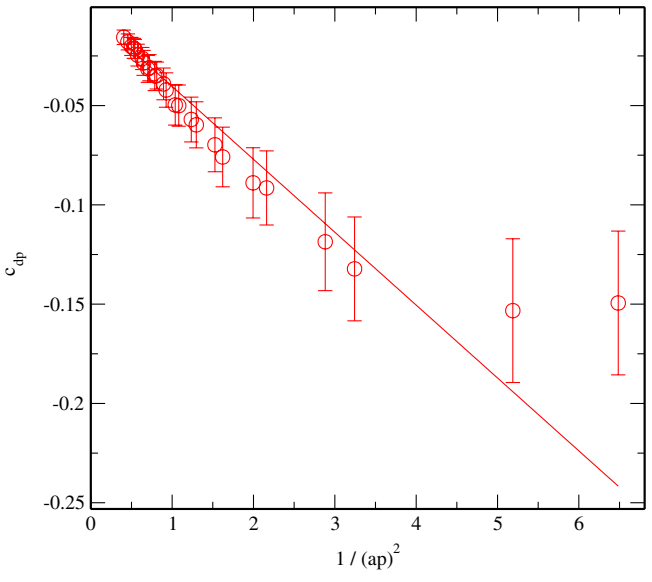

FIG. 14 (color online). Momentum dependence of the double pole coefficient, c_{dp}, fit to the expected p^{-2} behavior. Good agreement is seen.

the complete partially quenched results for each of our four sources.

F. Mass renormalization and renormalization group running

To calculate the mass renormalization constant Z_m, as defined in Eq. (16), we can either directly take the derivative of $\mathrm{Tr}[S^{-1}(p)]$, by following Eq. (22),

$$Z_m Z_q = \frac{1}{12} \frac{\partial\, \mathrm{Tr}[S^{-1}]}{\partial m_{\rm val}} \tag{45}$$

or we can use the Ward-Takahashi identity,

$$Z_m = \frac{1}{Z_S}. \tag{46}$$

With the analysis described in the above sections, we find that the method with the smallest statistical uncertainty is to use $1/Z_S$ as the value of Z_m. To remove the factor Z_q from Z_q/Z_S (which is equal to Λ_S and can be calculated as described in Section IV B), we use the ratio Z_q/Z_A calculated in Sec. IV C, as well as the value Z_A. This quantity has been determined in earlier work by using a ratio of matrix elements between hadronic states involving the partially conserved, 5-dimensional, DWF axial current which has a known normalization. (Note, using the more direct approach of determining Z_q from the large momentum behavior of the quark propagator leads to a result for Z_q with considerably larger errors [8].) Results for Z_A from $16^3 \times 32$ [$Z_A = 0.7162(2)$] and $24^3 \times 64$ ($Z_A = 0.7161(1)$) volumes can be found in Refs. [2,5] respectively. Here we use the latter, more accurate value. We therefore determine Z_m in the RI/MOM scheme by computing separately the three factors on the right-hand side of

$$Z_m^{\rm RI/MOM}(p) = \left[\frac{Z_q}{Z_S}(p)\right]\left[\frac{Z_A}{Z_q}(p)\right]\left(\frac{1}{Z_A}\right). \tag{47}$$

Table XII contains the values of $Z_m^{\rm RI/MOM}(p)$ for a variety of momentum scales.

After obtaining the lattice value of $Z_m^{\rm RI/MOM}$ at different momenta, we divide it by the predicted renormalization group running factor to calculate the scale-invariant quantity $Z_m^{\rm SI}$. The four-loop running formula we use is [15]:

$$Z_m^{\rm SI} = \frac{c(\alpha_s(\mu_0)/\pi)}{c(\alpha_s(\mu)/\pi)} Z_m^{\rm RI/MOM}(\mu) \tag{48}$$

where μ_0 is chosen such that $(a\mu_0)^2 = 2$, a value that lies within the fitting range used below. For completeness we present in the appendices the detailed procedure for running α_s at four-loops (Appendix A) and the form of running factors (Appendix B).

As Fig. 15 shows, the quantity $Z_m^{\rm SI}$ is remarkably independent of the scale μ. However, in spite of the name, for other cases, the scale-invariant Z factors do show noticeable scale dependence and an additional correction is

TABLE XII. The nonperturbative factor $Z_m^{\mathrm{RI/MOM}}$ as a function of the scale μ calculated from Λ_S and the corresponding values for $Z_m^{\overline{\mathrm{MS}}}$. Note that the values for $Z_m^{\overline{\mathrm{MS}}}$ given in column three are obtained from those in column two by applying the RI/MOM $-$ $\overline{\mathrm{MS}}$ perturbative matching factors after the $O(a\mu)^2$ lattice artifacts have been removed using an intermediate conversion to a scale-invariant scheme as described in the text.

μ(GeV)	$Z_m^{\mathrm{RI/MOM}}$	$Z_m^{\overline{\mathrm{MS}}}$
1.018	2.85(18)	1.625(47)
1.358	2.56(11)	1.758(51)
1.556	2.428(80)	1.731(51)
1.796	2.273(56)	1.690(49)
1.920	2.216(49)	1.669(49)
2.037	2.146(42)	1.651(48)
2.147	2.087(37)	1.634(48)
2.352	2.018(29)	1.605(47)
2.448	1.978(27)	1.593(46)
2.716	1.899(22)	1.562(46)

warranted. (See, for example, Fig. 17.) We believe that the primary reason for this lack of scale invariance is the presence of lattice artifacts, namely, the finite lattice spacing which introduces a small error of $\mathcal{O}((a\mu)^2)$. Such an error can be reduced by removing the μ^2 dependence in Z_m^{SI}. To do this we fit this momentum-dependent Z_m^{SI} to the form $A + B(a\mu)^2$ over the momentum range $1.3 < (a\mu)^2 < 2.5$ and then take the $(a\mu)^2 \to 0$ limit of that fit to remove the μ^2 momentum dependence. We interpret the outcome as the *true* Z_m^{SI}. Note, we are ignoring possible μ dependence arising from the absence of higher order terms in the matching factor. Such scale dependence can only be removed by even higher order computation of the perturbative matching factor and such a correction is expected to be very small. While this procedure represents a negligible correction for this case of Z_m^{SI}, it will have a more significant effect in the cases considered below.

Our ultimate goal is to determine $Z_m^{\overline{\mathrm{MS}}}$ which connects the bare lattice quark mass to its continuum counterpart defined according to the $\overline{\mathrm{MS}}$ scheme, at the renormalization scale $\mu = 2$ GeV, because the corresponding continuum renormalization is conventionally done in this scheme. So we again use Eq. (48) to calculate $Z_m^{\mathrm{RI/MOM}}$ (2 GeV) from the scale-independent value of Z_m^{SI}. Then we multiply it with the three-loop matching factor, which will also be explained in Appendix B, to match the $Z_m^{\mathrm{RI/MOM}}$ (2 GeV) to the $\overline{\mathrm{MS}}$ scheme. The final step is shown in Fig. 16 and the results are given in Table XII. The renormalization constant at the desired scale is

$$Z_m^{\overline{\mathrm{MS}}}(2\ \mathrm{GeV}) = 1.656 \pm 0.048(\mathrm{stat}) \pm 0.150(\mathrm{sys}). \quad (49)$$

As for other such combined quantities, the statistical error is obtained by applying the jackknife procedure to the product of the two ratios in Eq. (47). (The statistical errors on Z_A are negligible). The systematic error is determined by adding in quadrature our estimates of three different types of systematic error which we will now discuss.

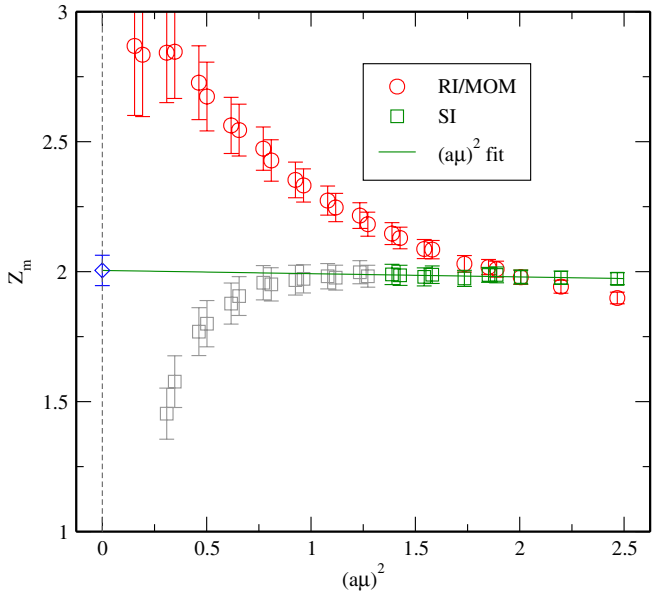

FIG. 15 (color online). The quantities $Z_m^{\mathrm{RI/MOM}}(\mu)$ and $Z_m^{\mathrm{SI}}(\mu)$ plotted versus the square of the scale $a\mu$. Here $Z_m^{\mathrm{SI}}(\mu)$ is obtained by dividing $Z_m^{\mathrm{RI/MOM}}(\mu)$ by the predicted perturbative running factor. Shown also is the linear extrapolation of $Z_m^{\mathrm{SI}}(\mu) = Z_m^{\mathrm{SI}} + c(a\mu)^2$ using the momentum region $1.3 < (a\mu)^2 < 2.5$ to remove lattice artifacts.

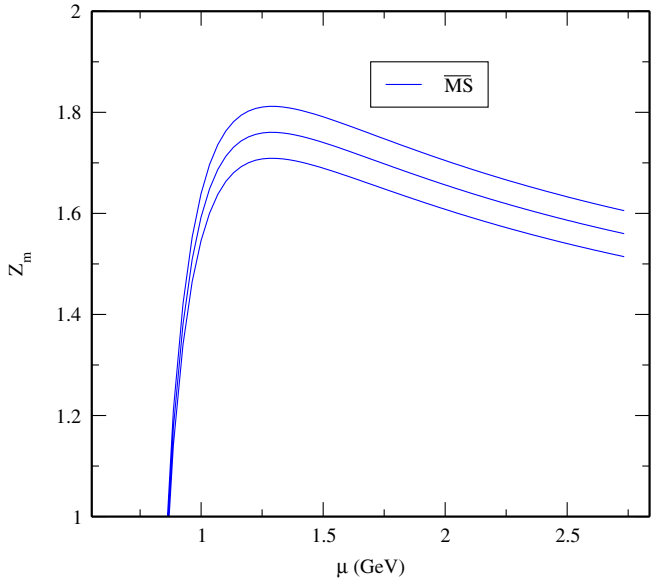

FIG. 16 (color online). The mass renormalization factor Z_m expressed in the $\overline{\mathrm{MS}}$ scheme. These results are obtained by applying the perturbative running factor to Z_m^{SI}. The value we are interested in is $Z_m^{\overline{\mathrm{MS}}}(\mu = 2\ \mathrm{GeV})$. The upper and lower curves show the statistical errors.

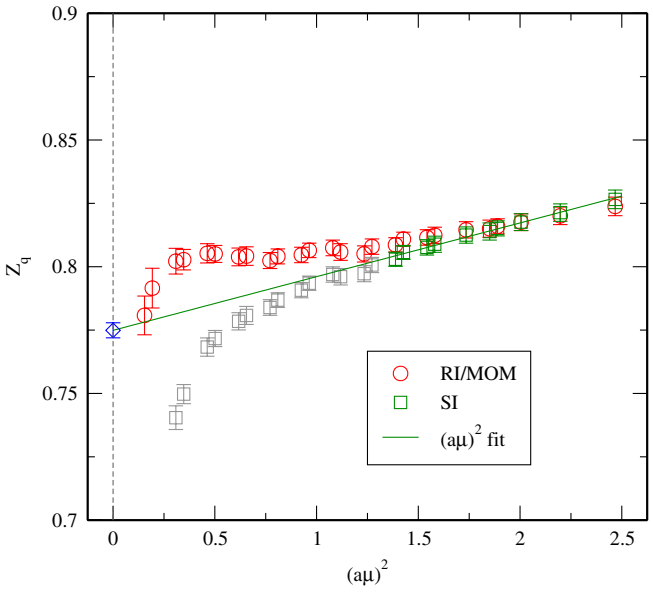

FIG. 17 (color online). The quantities $Z_q^{\mathrm{RI/MOM}}(\mu)$ and $Z_q^{\mathrm{SI}}(\mu)$ plotted versus the square of the scale $a\mu$. Here $Z_q^{\mathrm{SI}}(\mu)$ is obtained by dividing $Z_q^{\mathrm{RI/MOM}}(\mu)$ by the predicted perturbative running factor. Shown also is the linear extrapolation of $Z_q^{\mathrm{SI}}(\mu) = Z_q^{\mathrm{SI}} + c(a\mu)^2$ using the momentum region $1.3 < (a\mu)^2 < 2.5$ to remove lattice artifacts.

The first is the effect on Z_m of the difference between determining Z_q/Z_A from $\frac{1}{2}(\Lambda_A + \Lambda_V)$ or from Λ_A. This contributes an error of ± 0.011 to $Z_m^{\overline{\mathrm{MS}}}(2\ \mathrm{GeV})$. Next we must assign an error to our use of three-loop matching factor, given in Eq. (B6). Here we assign an error equal to the magnitude of the final, order α_s^3 error in this perturbative expression, which is ± 0.103. While this may be a conservative estimate of the omitted terms of order α_s^4 and higher, it also is intended to include the errors introduced by the order α_s^3 estimate of the perturbative running determine the intermediate SI step used to remove the $(a\mu)^2$ errors.

Finally we address the errors arising from our failure to extrapolate to the limit of vanishing strange quark mass. Recall, we have evaluated the chiral limit in which both the valence quark mass which enters our off-shell propagators and the dynamical light quark mass are extrapolated to zero. However, all of the gauge ensembles used in this calculation were computed with a nonzero strange quark mass $m_s = 0.04$. Since we are matching our Green functions to those computed in perturbation theory in the mass-independent, $m \to 0$, limit our nonzero value for m_s implies an additional systematic error. Because the dynamical quarks enter only through loops, their effect is different from that of the valence quarks discussed above. They do not contribute chiral symmetry breaking effects in our matrix elements. However, because of low-energy chiral symmetry breaking, we do expect the dynamical quark masses to appear linearly in a quantity such as Z_m in the limit $m \to 0$. To estimate the size of this $O(m_s)$ effect, we begin with the size of the observed linear dependence, $\partial Z_m/\partial m \approx 5.4$ which comes from both the calculated valence and light dynamical mass dependence of Λ_S. This is then multiplied by $1/2$ because there is only one flavor of strange quark and by $m_s = 0.04$ giving an error in Z_m of ± 0.108. The total systematic error given in Eq. (49), ± 0.150, is then the sum of these three errors in quadrature.

G. Quark wave function renormalization and renormalization group running

In Sec. IV C, we calculated the ratio of renormalization constants

$$\frac{Z_q}{Z_A} = \frac{1}{2}(\Lambda_A + \Lambda_V). \tag{50}$$

To calculate Z_q, we multiply this quantity with $Z_A = 0.7161(1)$ obtained in Ref. [5]. Thus, we have evaluated the quantity Z_q in the RI/MOM scheme, which is shown in Table XIII. To calculate Z_q in the $\overline{\mathrm{MS}}$ scheme, we follow a similar procedure as in the previous section, and start by dividing $Z_q^{\mathrm{RI/MOM}}$ by the perturbative running factor. As shown in Appendix C, the functional form of the running factor is quite similar to that of Z_m. The energy scale μ_0 where Z_q^{SI} is fixed to the $Z_q^{\mathrm{RI/MOM}}$ value is again chosen such that $(a\mu_0)^2 = 2$.

The calculated values of Z_q^{SI} vary slightly with momentum due to the presence of lattice artifacts. To remove these, we again fit the dependence to the form $A + B(a\mu)^2$ and extrapolate to $a = 0$. The procedure is shown in Fig. 17. Finally, we take the scale-invariant Z_q^{SI}, run up to different scales in the RI/MOM scheme, and then apply the perturbative matching factor (Appendix C) to translate it to

TABLE XIII. The nonperturbative factor $Z_q^{\mathrm{RI/MOM}}$ as a function of the scale μ calculated from $\frac{1}{2}(\Lambda_A + \Lambda_V)$ and the corresponding values for $Z_q^{\overline{\mathrm{MS}}}$. Note that the values for $Z_q^{\overline{\mathrm{MS}}}$ given in column three are obtained from those in column two by applying the RI/MOM $-$ $\overline{\mathrm{MS}}$ perturbative matching factors after the $O(a\mu)^2$ lattice artifacts have been removed using an intermediate conversion to a scale-invariant scheme as described in the text.

μ(GeV)	$Z_q^{\mathrm{RI/MOM}}$	$Z_q^{\overline{\mathrm{MS}}}$
1.018	0.8028(40)	0.8010(31)
1.358	0.8039(35)	0.7849(30)
1.556	0.8041(30)	0.7798(30)
1.796	0.8074(31)	0.7754(30)
1.920	0.8050(32)	0.7736(30)
2.037	0.8086(28)	0.7722(30)
2.147	0.8115(31)	0.7710(30)
2.352	0.8150(34)	0.7691(29)
2.448	0.8176(33)	0.7684(29)
2.716	0.8238(37)	0.7665(29)

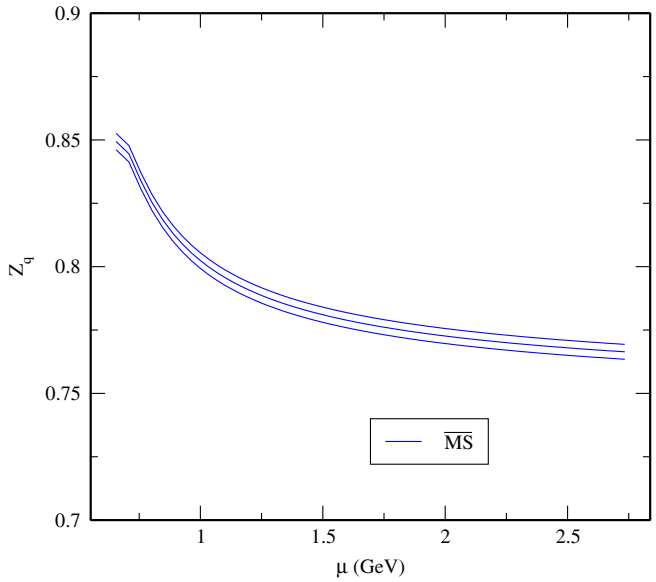

FIG. 18 (color online). The wave function renormalization factor Z_q expressed in the $\overline{\text{MS}}$ scheme. These results are obtained by applying the perturbative running factor to Z_q^{SI}. The value we are interested in is $Z_q^{\overline{\text{MS}}}(\mu = 2\ \text{GeV})$. The upper and lower curves show the statistical errors.

the $\overline{\text{MS}}$ scheme. The $\overline{\text{MS}}$ values are shown in Fig. 18 and Table XIII. Of particular interest, the value at $\mu = 2$ GeV is

$$Z_q^{\overline{\text{MS}}}(2\ \text{GeV}) = 0.7726 \pm 0.0030(\text{stat}) \pm 0.0083(\text{sys}) \tag{51}$$

The systematic errors are estimated using the same procedure explained in Sec. IV F. They are the sum in quadrature of the estimated errors arising from the difference $\Lambda_A - \Lambda_V$ (0.0061), the use of a perturbative matching factor accurate to order α^3 (0.0045) and our use of a nonzero sea quark mass (0.0035).

H. Tensor current renormalization and renormalization group running

To calculate the tensor current renormalization constant Z_T, we follow a procedure similar to those of the previous two sections. For each dynamical quark mass, we combine the ratios Z_q/Z_T and Z_q/Z_A in order to obtain the ratio of Z_T to Z_A in the RI/MOM scheme:

$$\frac{Z_T^{\text{RI/MOM}}}{Z_A}(p) = \left[\frac{Z_T}{Z_q}(p)\right]\left[\frac{Z_q}{Z_A}(p)\right].$$

Ultimately, we use the independent hadronic matrix element calculation of Z_A, which gives $Z_A = 0.7161(1)$, to obtain Z_T. Table XIV shows the values obtained for the $Z_T^{\text{RI/MOM}}$ in the chiral limit for a range of lattice momenta. As discussed above we have performed the chiral extrapolation using a linear functional form, and Fig. 19 shows this

TABLE XIV. The nonperturbative factor $Z_T^{\text{RI/MOM}}$ as a function of the scale μ calculated from Λ_T and the corresponding values for $Z_T^{\overline{\text{MS}}}$. Note that the values for $Z_T^{\overline{\text{MS}}}$ given in column three are obtained from those in column two by applying the RI/MOM $-$ $\overline{\text{MS}}$ perturbative matching factors after the $O(a\mu)^2$ lattice artifacts have been removed using an intermediate conversion to a scale-invariant scheme as described in the text.

μ(GeV)	$Z_T^{\text{RI/MOM}}$	$Z_T^{\overline{\text{MS}}}$
1.018	0.9121(74)	0.8812(38)
1.358	0.8583(46)	0.8355(36)
1.556	0.8380(32)	0.8194(35)
1.796	0.8177(27)	0.8048(34)
1.920	0.8118(27)	0.7986(34)
2.037	0.8037(22)	0.7935(34)
2.147	0.7981(21)	0.7892(34)
2.352	0.7899(18)	0.7821(33)
2.448	0.7862(17)	0.7791(33)
2.716	0.7779(16)	0.7719(33)

linear extrapolation at the lattice momentum $(ap)^2 = 1.388$.

We obtain SI values for Z_T in the chiral limit by dividing out the tensor current perturbative running factor, the evaluation of which is described in Appendix E. Again, the SI values obtained in this way exhibit a dependence on the lattice momenta, and again we fit the momentum-dependent Z_T^{SI} to the form $A + B(a\mu)^2$ and extrapolate to $(a\mu)^2 \to 0$ to remove the lattice artifacts, as shown in Fig. 20. Finally, we run the scale-invariant Z_T/Z_A back to different scales in the RI/MOM scheme and use the perturbative matching factor (Appendix E) to match to the $\overline{\text{MS}}$ scheme. The $\overline{\text{MS}}$ values are shown in Fig. 21 and

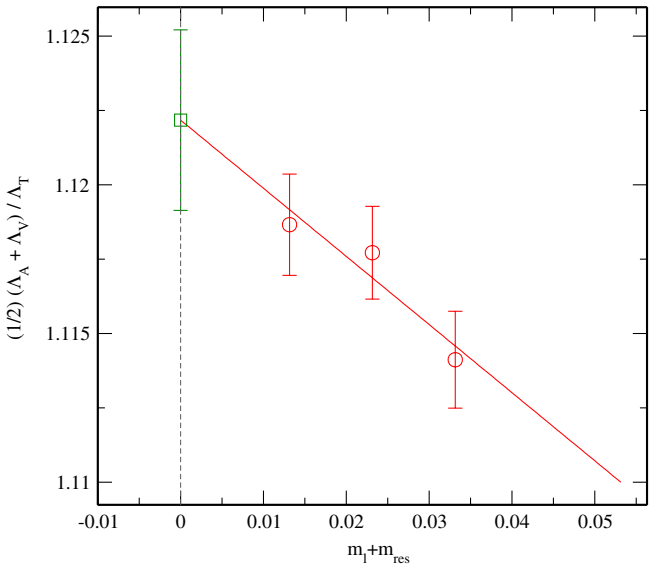

FIG. 19 (color online). A plot of $\frac{1}{2}(\Lambda_A + \Lambda_V)/\Lambda_T$ as a function of quark mass as well as the linear extrapolation to the chiral limit, at $(ap)^2 = 1.388$, or $\mu = 2.04$ GeV.

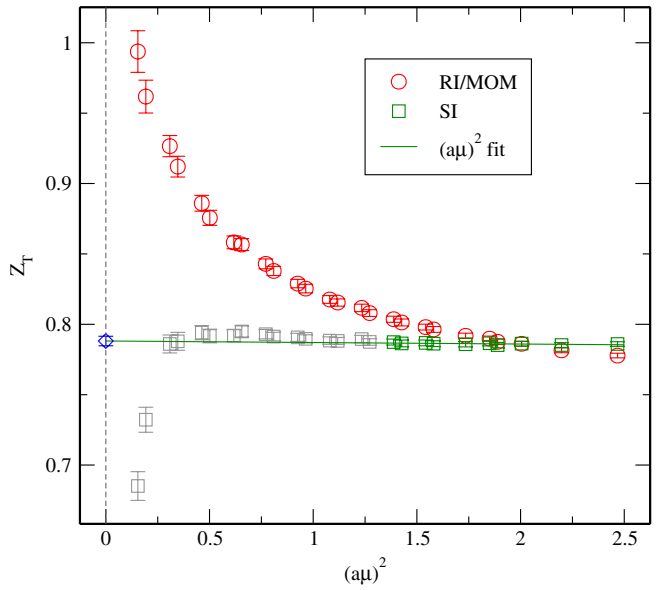

FIG. 20 (color online). The quantities $Z_T^{\mathrm{RI/MOM}}(\mu)$ and $Z_T^{\mathrm{SI}}(\mu)$ plotted versus the square of the scale $a\mu$. Here $Z_T^{\mathrm{SI}}(\mu)$ is obtained by dividing $Z_T^{\mathrm{RI/MOM}}(\mu)$ by the predicted perturbative running factor. Shown also is the linear extrapolation of $Z_T^{\mathrm{SI}}(\mu) = Z_T^{\mathrm{SI}} + c(a\mu)^2$ using the momentum region $1.3 < (a\mu)^2 < 2.5$ to remove lattice artifacts.

Table XIV. At $\mu = 2$ GeV, we obtain:

$$Z_T^{\overline{\mathrm{MS}}}(2\ \mathrm{GeV}) = 0.7950 \pm 0.0034(\mathrm{stat}) \pm 0.0150(\mathrm{sys}).$$

The systematic errors are determined in the same fashion as in the previous two sections. Specifically the errors arising from the difference $\Lambda_A - \Lambda_V$ (0.0054), the use of a perturbative matching factor accurate to order α (0.014) and our use of a nonzero sea quark mass (0.0003) are added in quadrature.

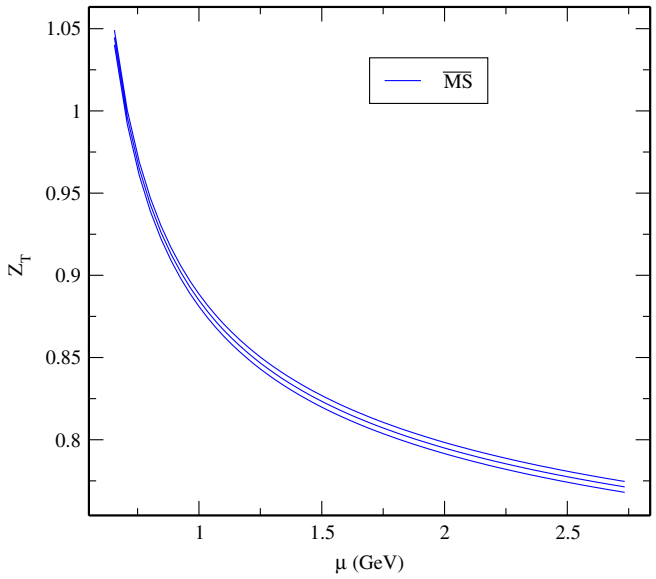

FIG. 21 (color online). The wave function renormalization factor Z_T expressed in the $\overline{\mathrm{MS}}$ scheme. These results are obtained by applying the perturbative running factor to Z_T^{SI}. The value we are interested in is $Z_T^{\overline{\mathrm{MS}}}(\mu = 2\ \mathrm{GeV})$. The upper and lower curves show the statistical errors.

V. RENORMALIZATION COEFFICIENTS FOR B_K

A. General procedure for computing the mixing coefficients

By the renormalization of B_K we mean the calculation of the renormalization coefficient for the operator

$$\mathcal{O}_{VV+AA} = (\bar{s}\gamma^\mu(1-\gamma_5)d)(\bar{s}\gamma_\mu(1-\gamma_5)d) \tag{52}$$

which is the operator responsible for the mixing between K^0 and $\bar{K}^0$. Since for finite L_s our theory does not posses exact chiral symmetry we must consider the possibility that this operator can mix with the four other $\Delta S = 2$ operators with a different chiral structure:

$$\mathcal{O}_{VV-AA} = (\bar{s}\gamma^\mu(1-\gamma_5)d)(\bar{s}\gamma_\mu(1+\gamma_5)d) \tag{53}$$

$$\mathcal{O}_{SS+PP} = (\bar{s}(1-\gamma_5)d)(\bar{s}(1-\gamma_5)d) \tag{54}$$

$$\mathcal{O}_{SS-PP} = (\bar{s}(1-\gamma_5)d)(\bar{s}(1+\gamma_5)d) \tag{55}$$

$$\mathcal{O}_{TT} = (\bar{s}\sigma^{\mu\nu}d)(\bar{s}\sigma_{\mu\nu}d) \tag{56}$$

where they are labeled by the chirality structure of the even-parity components. The odd-parity components of these operators are not important here since they do not contribute to $K^0 \leftrightarrow \bar{K}^0$ mixing.

For domain-wall fermions, the mixing of $\mathcal{O}_{VV+AA}$ with these four operators with wrong chirality should be strongly suppressed by $\mathcal{O}(m_{\mathrm{res}}^2)$. However, chiral perturbation theory predicts that the B parameters of the operators with the wrong chirality diverge in the chiral limit [16,17]. To address this issue, we will describe a theoretical argument to estimate the size of the mixing terms and an actual calculation of these chirality-violating mixing coefficients on the $2+1$ flavor dynamical lattices.

Following the Rome-Southampton prescription [4,16], we first calculate the 5×5 matrix,

$$M_{ij} = \hat{P}_j[\Gamma_i^{\mathrm{latt}}] = (\Gamma_i^{\mathrm{latt}})_{\alpha\beta\gamma\delta}^{ABCD}(\hat{P}_j)_{\beta\alpha\delta\gamma}^{BADC} \tag{57}$$

where Γ_i^{latt} is the amputated, four-point Green function. The Green functions are first averaged over all sources and configurations, and then amputated using the averaged propagator, in a procedure similar to the calculation of two-point amputated Green functions $\Pi_{\Gamma,0}(p)$ in Sec. IV B. $\hat{P}_j$ is a suitable projector, which projects out the component with the expected chirality (for example, the projector corresponding to $\mathcal{O}_{VV+AA}$ is $\gamma^\mu \otimes \gamma_\mu + \gamma^\mu\gamma_5 \otimes \gamma_\mu\gamma_5$). The subscripts $i, j \in \{VV+AA, VV-AA, SS-PP, SS+PP, TT\}$.

It is straightforward to calculate the mixing matrix at tree level which we denote as

$$F_{ij} = \hat{P}_j[\Gamma_i^{\text{tree}}]. \tag{58}$$

The RI/MOM renormalization condition which we adopt is then

$$\frac{1}{Z_q^2} Z_{ij} M_{jk} = F_{ik} \tag{59}$$

or

$$\frac{1}{Z_q^2} Z = F M^{-1}. \tag{60}$$

B. Theoretical argument for the suppression of mixing coefficients

As can be seen from the structure of the four operators in Eqs. (53)–(56), if they are to mix with $\mathcal{O}_{VV+AA}$ defined in Eq. (52) then two quark fields much change chirality from left- to right-handed. For domain wall fermions such a mixing can arise from the explicit breaking of chiral symmetry coming from the finite separation between the left and right walls. The asymptotic behavior for large L_s of the resulting mixing coefficients can be estimated using the transfer matrix T for propagation in the s-direction introduced by Furman and Shamir [12]. The large-L_s limit is then controlled by matrix elements of the operator T^{L_s} and is dominated by those four-dimensional fermion modes corresponding to eigenvalues of the transfer matrix which lie near unity.

As described in detail in Ref. [18] and in the original references cited therein, these fermion modes are believed to fall into two classes: modes localized in space-time with corresponding T eigenvalues falling arbitrarily close to unity and delocalized modes characterized by a mobility edge $\lambda_c > 0$ and with eigenvalues of T lying below $e^{-\lambda_c}$ [19–22]. Since two quarks must change chirality to produce the required operator mixing, for the case of delocalized modes such mixing will be suppressed by the two factors of $e^{-\lambda_c L_s}$ needed for the propagation between the left and right walls of these two fermions, consistent with our estimate above that such effects should be of order m_{res}^2.

However, the effects of the localized modes are more subtle. We must address the possibility raised by Golterman and Shamir [23] that the contribution of such a mode to m_{res} is suppressed because such modes are relatively rare and the necessary coincidence with the location of the operators being mixed is unlikely. However, if present, such a mode can mix right- and left-handed fermions with little further suppression since the corresponding T eigenvalue may be very close to unity. This raises the possibility that a single such mode, suppressed by a single factor of m_{res} might be occupied by the two different quark flavors to provide the double chirality flip needed to mix the operators. Fortunately, as argued in Refs. [9,16], this is not possible because the mixing in question requires both a quark and an antiquark or two quarks of the same flavor to propagate across the fifth dimension. This requires two distinct modes and hence incurs the double suppression which is well represented by the m_{res}^2 estimate above. Note, $m_{\text{res}}^2 \approx 10^{-5}$ which will introduce $O(0.1\%)$ errors in current calculations of B_K [24] and will be too small to be seen in nonperturbative studies presented here.

C. Lattice calculation of mixing coefficients

With the procedure described in Sec. VA, we can directly calculate the mixing coefficients. In particular, we have calculated the off-diagonal terms in the matrix FM^{-1}. Figure 22 shows the mixing coefficient $FM^{-1}_{VV+AA,VV-AA}$ at different unitary masses. As in the earlier discussion of the $\Lambda_A - \Lambda_V$ difference, our use of exceptional external momenta permits both a linear and quadratic mass dependence. As was found in Ref. [16] and suggested by the mass dependence seen in Fig. 23 a linear dependence appears reasonable and it is a linear form that we have used in determining the chiral limit shown in Fig. 22.

As can be seen in Fig. 22, at the chosen reference scale, $\mu \simeq 2$ GeV or $(ap)^2 \simeq 1.4$, the mixing coefficient is about 0.7% and decreases when the scale is made larger. Similar to the discussion in Sec. IV C, we again propose that this nonzero mixing coefficient in the chiral limit has its source in our use of exceptional momenta. Again we can determine the asymptotic behavior of the amplitude in question by determining the least negative degree of divergence of a

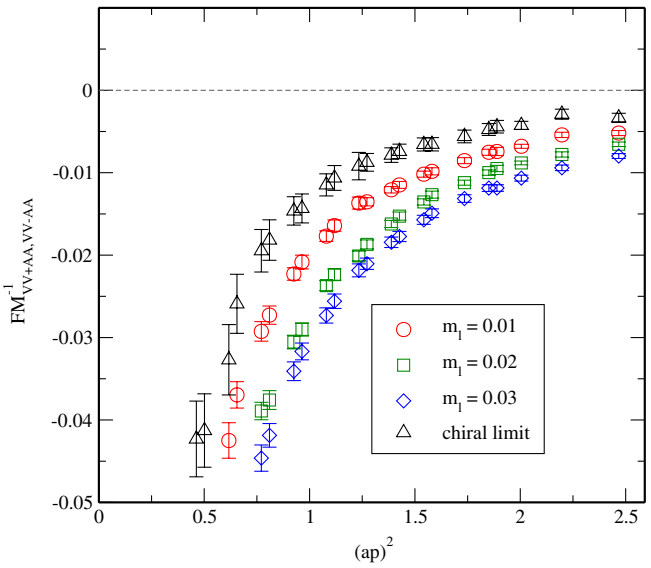

FIG. 22 (color online). The mixing coefficient $FM^{-1}_{VV+AA,VV-AA}$ for our three unitary mass values and linearly extrapolated to the chiral limit.

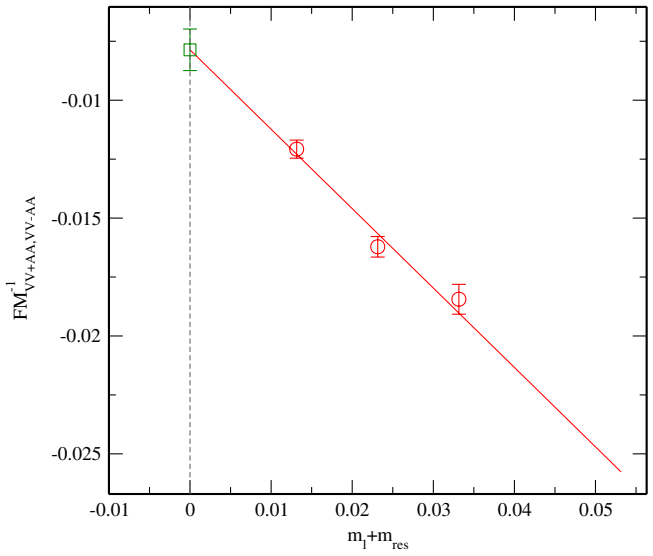

FIG. 23 (color online). Linear extrapolation of the mixing coefficient $FM^{-1}_{VV+AA,VV-AA}$ to the chiral limit using the three unitary mass values, at the momentum scale $\mu = 2.04$ GeV.

subgraph Γ' through which all of the large external momenta can be arranged to flow. Here it is convenient to treat the operator O_{LL}, which is evaluated at zero momentum, as an internal vertex of dimension 6 rather than an unusual sort of external line. This alters the rules for computing the degree of divergence of a subgraph: now any connected subgraph with F external fermion lines and B external boson lines in which this new O_{LL} vertex appears, must have degree of divergence $d = 6 - 3F/2 - B$ since O_{LL} has a dimension two higher than the usual renormalizable coupling. (As before, the degree of divergence of a disconnected graph is the sum of the degrees of divergence of its connected components.)

As in the case of the vertex amplitude discussed in Sec. IV C, the appearance of exceptional momenta does not change the asymptotic behavior in the large λ limit with external momenta λp_i for $1 \le i \le 4$. Even for our exceptional case $p_1 = p_3 = -p_2 = -p_4$, λ^d scaling with $d = 6 - 4 \cdot 3/2 = 0$ is expected. However, derivatives with respect to the quark mass or the occurrence of factors of $\langle \bar{q}q \rangle$ will be strongly affected by this choice of external momenta. As is shown in Fig. 24, we can identify a disconnected subgraph Γ' through which all the large external momenta can be routed which has $d = (6 - 4 \cdot 3/2) + (4 - 4 \cdot 3/2) = -2$. (Note, momentum conservation implies that if all of the large momenta can be routed within a disconnected diagram then the choice of external momenta must be exceptional.) This $d = -2$ value implies a $1/p^2$ behavior with only low momenta flowing through the omitted subgraph Γ_1. Since Γ_1 has four external lines it can translate standard QCD vacuum symmetry breaking into the chiral symmetry breaking that is required to produce the operator mixing shown in Fig. 22.

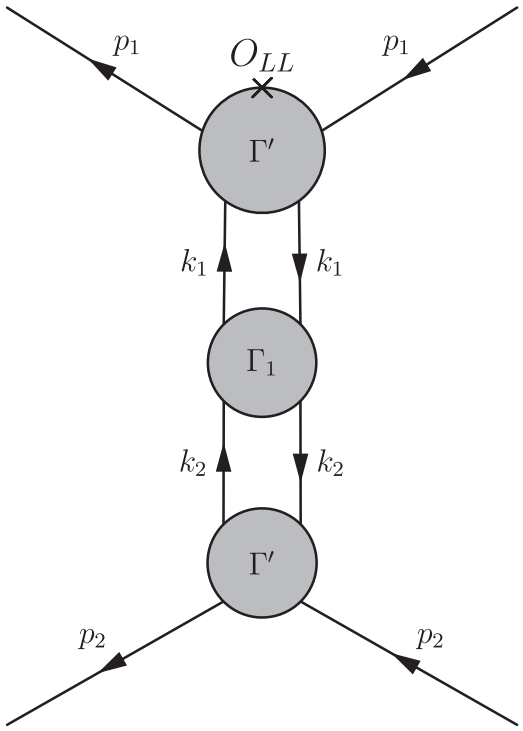

FIG. 24. A possible identification of subgraphs appearing in the chirality violating mixing between O_{LL} and other four-quark operators. The disconnected subdiagram Γ' has degree of divergence $d = -2$ for the case of exceptional momenta shown here. This permits a complex pattern of low-energy, vacuum chiral symmetry breaking coming from the low-energy, four-quark subgraph Γ_1 to enter such an amplitude with only a mild $1/p^2$ suppression.

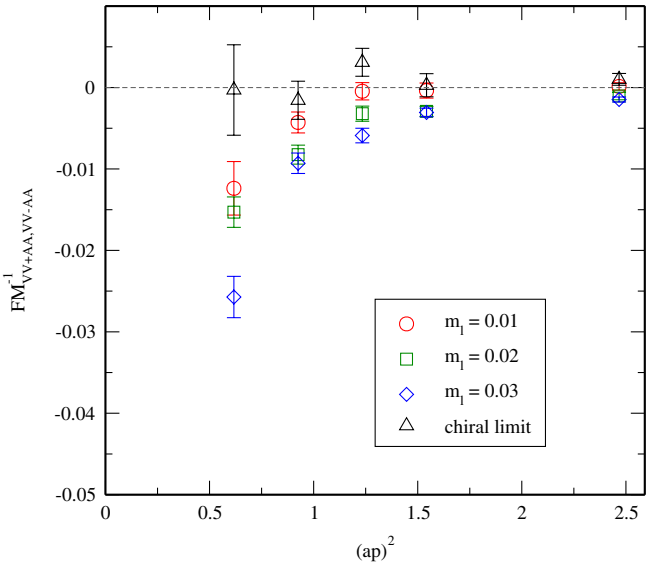

FIG. 25 (color online). The mixing coefficient $FM^{-1}_{VV+AA,VV-AA}$ calculated at nonexceptional momenta. When extrapolated to the chiral limit the mixing coefficient vanishes, which shows that chiral symmetry breaking as shown in Fig. 22 comes from the existence of a low-energy subdiagram that enters because of the special choice of external momenta.

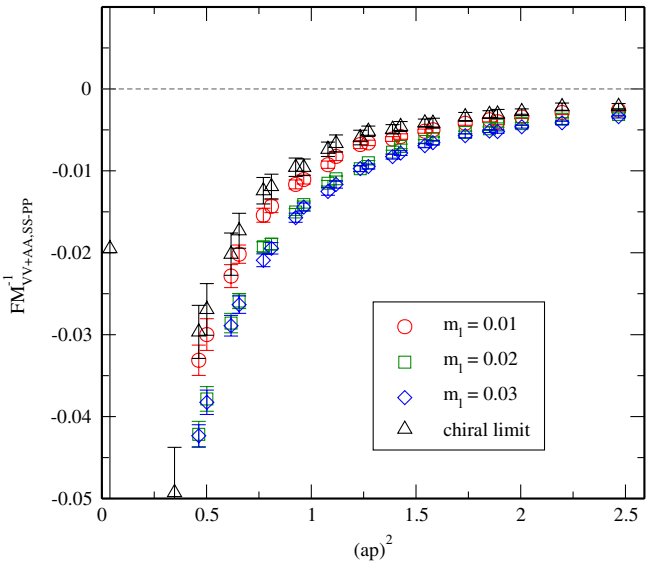

FIG. 26 (color online). The mixing coefficient $FM^{-1}_{VV+AA,SS-PP}$ for unitary choices of the mass.

Again, we confirm this conclusion, by recomputing the coefficient $FM^{-1}_{VV+AA,VV-AA}$ at nonexceptional momenta, as shown in Fig. 25. With that choice of momenta the mixing coefficient vanishes completely within our statistical accuracy.

The other chiral symmetry breaking mixing coefficients, $FM^{-1}_{VV+AA,SS\pm PP}$ and $FM^{-1}_{VV+AA,TT}$ are very similar to the case of $FM^{-1}_{VV+AA,VV-AA}$ just discussed. These coefficients

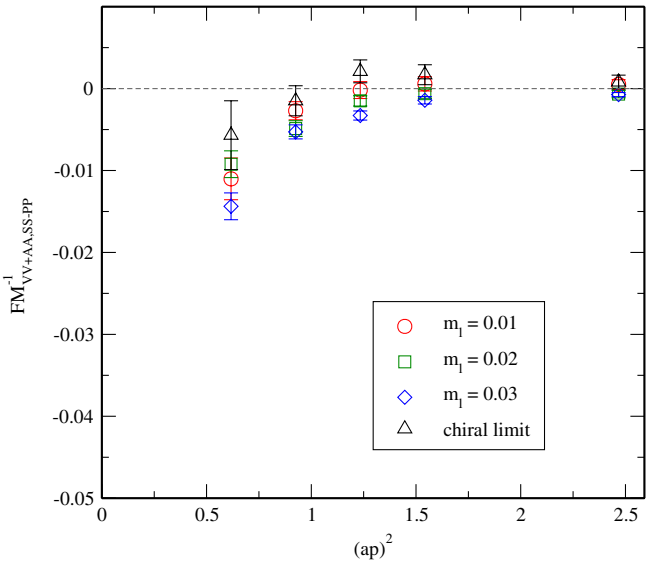

FIG. 27 (color online). The mixing coefficient $FM^{-1}_{VV+AA,SS-PP}$ calculated at nonexceptional momenta. When extrapolated to the chiral limit the mixing coefficient vanishes, which shows that chiral symmetry breaking as shown in Fig. 26 comes from the existence of a low-energy subdiagram that enters because of the special choice of external momenta.

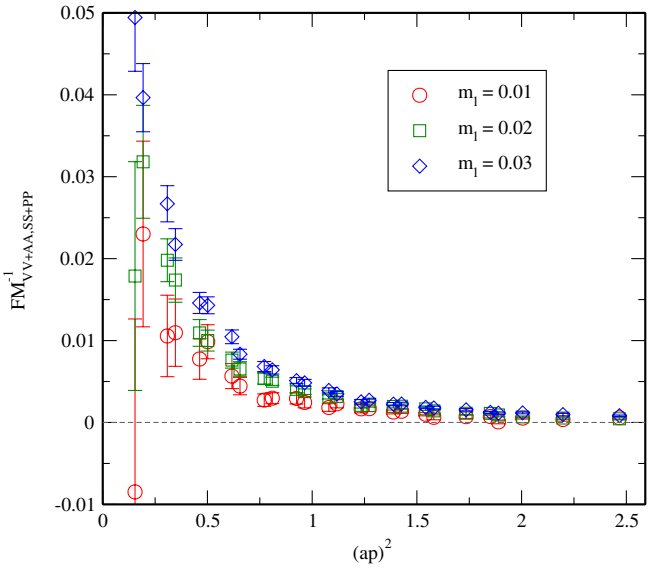

FIG. 28 (color online). The mixing coefficient $FM^{-1}_{VV+AA,SS+PP}$ for unitary choices of the mass. The coefficients are very tiny over the region of medium to large momenta.

are plotted in Figs. 26–29. Since our theoretical argument implies that the mixing coefficients are very small, i.e. $\mathcal{O}(m^2_{\rm res})$ and our numerical results are consistent with this implication, it is safe to neglect them and calculate the renormalization coefficient for B_K:

$$Z^{\rm RI/MOM}_{B_K} = \frac{Z_{VV+AA,VV+AA}}{Z^2_A}. \tag{61}$$

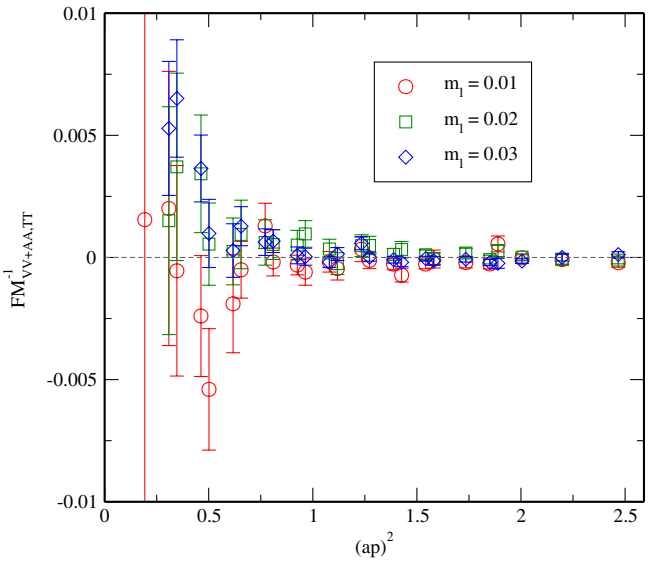

FIG. 29 (color online). The mixing coefficient $FM^{-1}_{VV+AA,TT}$ for unitary choices of the mass. These coefficients agree well with zero.

TABLE XV. The quantity $Z_{B_K}^{\mathrm{RI/MOM}}$ evaluated at the unitary points where $m_{\mathrm{val}} = m_l = m$.

μ(GeV)	$m = 0.01$	$m = 0.02$	$m = 0.03$
0.954	0.9663(69)	0.9737(52)	0.9538(44)
1.272	0.9347(39)	0.9387(35)	0.9315(30)
1.458	0.9266(31)	0.9289(30)	0.9245(26)
1.683	0.9189(25)	0.9189(25)	0.9167(24)
1.799	0.9151(22)	0.9137(23)	0.9126(23)
1.909	0.9114(23)	0.9106(22)	0.9102(22)
2.012	0.9085(22)	0.9077(20)	0.9078(21)
2.204	0.9045(23)	0.9026(20)	0.9035(21)
2.294	0.9018(20)	0.9004(19)	0.9020(20)
2.545	0.8974(21)	0.8953(19)	0.8978(19)

D. Calculation of Z_{B_K} and renormalization group running

Using Eq. (61), the value of Z_q/Z_A from Sec. IV C and the value of $Z_q^{-2} Z_{VV+AA,VV+AA} = F M^{-1}_{VV+AA,VV+AA}$, we can calculate the lattice values of Z_{B_K} at different masses and momenta, as shown in Table XV. To extrapolate to the chiral limit, we again use a linear function, for the same reasons as described in Section IV C. The linear mass fit at the scale $\mu = 2$ GeV is illustrated in Fig. 30, and the value of $Z_{B_K}^{\mathrm{RI/MOM}}$ in the chiral limit is shown in Fig. 31 and Table XVI.

Similar to the procedure described in Sec. IV F, in order to determine $Z_{B_K}^{\overline{\mathrm{MS}}}$ from $Z_{B_K}^{\mathrm{RI/MOM}}$, we first divide the $Z_{B_K}^{\mathrm{RI/MOM}}(\mu)$ by the predicted running factor at one-loop order and obtain the quantity $Z_{B_K}^{\mathrm{SI}}(\mu)$. Then we fit a quadratic function $A + B(a\mu)^2$ over the region $1.3 < (a\mu)^2 < 2.5$ to remove the $\mathcal{O}((a\mu)^2)$ dependence from $Z_{B_K}^{\mathrm{SI}}$ induced by the lattice artifacts. Finally, we restore its perturbative running in the $\overline{\mathrm{MS}}$ scheme to the scale $\mu = 2$ GeV. The perturbative running and matching factors are presented in Appendix D.

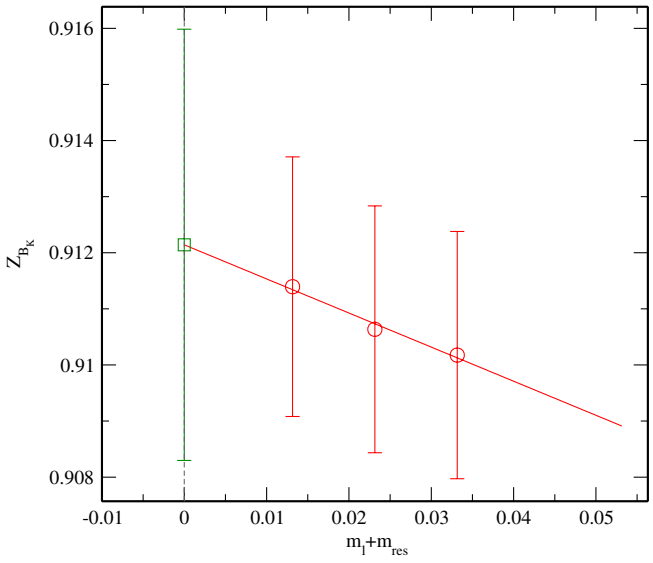

FIG. 30 (color online). Linear extrapolation of Z_{B_K} to the chiral limit using unitary mass values and the scale $\mu = 2.04$ GeV.

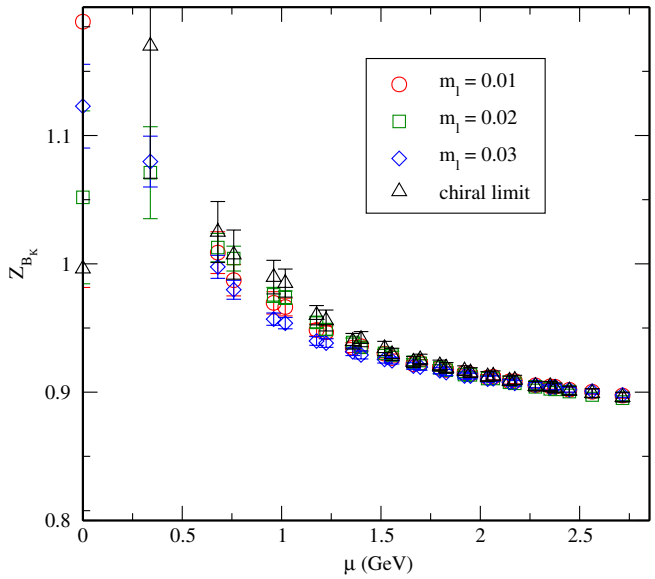

FIG. 31 (color online). The renormalization factor $Z_{B_K}^{\mathrm{RI/MOM}}$ evaluated for unitary mass values and extrapolated to the chiral limit.

The procedure of dividing by the running and removing the $(a\mu)^2$ dependence is shown in Fig. 32, and the result of restoring the running in the $\overline{\mathrm{MS}}$ scheme is shown in Fig. 33. As can be seen from Fig. 32, in the case of Z_{B_K} the correction for this discretization effect is on the 0.5% level and the fitted SI values are accurately linear over a larger

TABLE XVI. The nonperturbative factor $Z_{B_K}^{\mathrm{RI/MOM}}$ as a function of the scale μ and the corresponding values for $Z_{B_K}^{\overline{\mathrm{MS}}}$. Note that the values for $Z_{B_K}^{\overline{\mathrm{MS}}}$ given in column three are obtained from those in column two by applying the RI/MOM $-$ $\overline{\mathrm{MS}}$ perturbative matching factors after the $O(a\mu)^2$ lattice artifacts have been removed using an intermediate conversion to a scale-invariant scheme as described in the text.

μ(GeV)	$Z_{B_K}^{\mathrm{RI/MOM}}$	$Z_{B_K}^{\overline{\mathrm{MS}}}$
1.018	0.985(11)	1.0016(56)
1.358	0.9397(61)	0.9651(54)
1.556	0.9295(48)	0.9507(54)
1.796	0.9208(42)	0.9370(53)
1.920	0.9168(38)	0.9311(52)
2.037	0.9121(38)	0.9261(52)
2.147	0.9088(37)	0.9217(52)
2.352	0.9045(39)	0.9145(52)
2.448	0.9011(35)	0.9114(51)
2.716	0.8961(38)	0.9038(51)

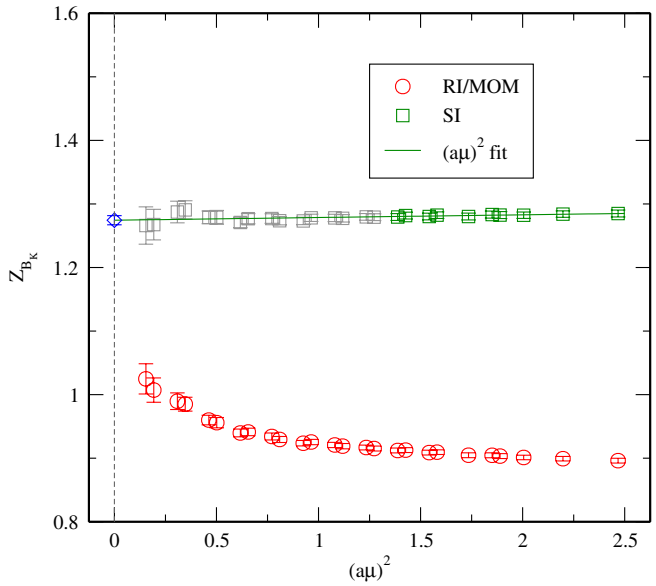

FIG. 32 (color online). The quantities $Z_{B_K}^{\mathrm{RI/MOM}}$ and $Z_{B_K}^{\mathrm{SI}}$ plotted versus the square of the scale $a\mu$. Here $Z_{B_K}^{\mathrm{SI}}$ is obtained by dividing $Z_{B_K}^{\mathrm{RI/MOM}}$ by the predicted perturbative running factor. Shown also is the linear extrapolation of $Z_{B_K}^{\mathrm{SI}}(\mu) = Z_{B_K}^{\mathrm{SI}} + c(a\mu)^2$ using the momentum region $1.3 < (a\mu)^2 < 2.5$ to remove lattice artifacts.

range of $(a\mu)^2$ than that used in the fit. Table XVI lists $Z_{B_K}^{\overline{\mathrm{MS}}}$ at different momentum scales. The final Z_{B_K} we obtain in the $\overline{\mathrm{MS}}$ scheme and $\mu = 2$ GeV is

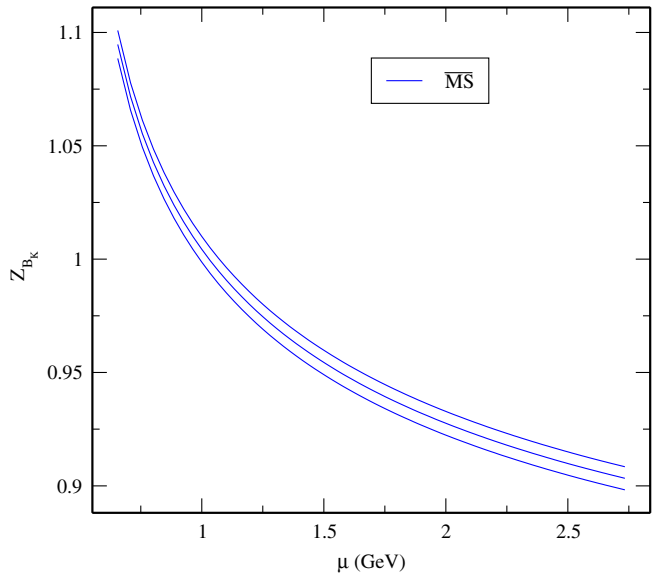

FIG. 33 (color online). The renormalization factor Z_{B_K} expressed in the $\overline{\mathrm{MS}}$ scheme. These results are obtained by applying the perturbative running factor to $Z_{B_K}^{\mathrm{SI}}$. The value we are interested in is $Z_{B_K}^{\overline{\mathrm{MS}}}(\mu = 2\ \mathrm{GeV})$. The upper and lower curves show the statistical errors.

$$Z_{B_K}^{\overline{\mathrm{MS}}}(2\ \mathrm{GeV}) = 0.9276 \pm 0.0052(\mathrm{stat}) \pm 0.0220(\mathrm{sys}). \tag{62}$$

The systematic error is calculated, following the same procedure as has been used for the previous quantities, as a sum in quadrature of the amount the result changes when $\frac{1}{2}(\Lambda_A + \Lambda_V)$ is replaced by Λ_A (0.0131), the size of the highest order perturbative correction being made [here of $O(\alpha_s)$] (0.0177) and the effect of our nonzero value for m_s in the calculation of Z_{B_K} (0.0007).

VI. CONCLUSIONS

We have presented a study of the renormalization coefficients Z_q, Z_m Z_T and B_K on the $16^3 \times 32$, $2 + 1$ flavor dynamical domain-wall fermion lattices with Iwasaki gauge action of $\beta = 2.13$ and $a^{-1} = 1.729(28)$ GeV generated by the RBC and UKQCD collaborations. These coefficients are important components in calculations of a number of important physical quantities reported elsewhere [3,24] The procedure closely follows that used in an earlier study with quenched lattice configurations [8,16]. In addition to providing the Z-factors necessary to support a variety of calculations on these lattice configurations, this paper also presents a number of new results which go beyond earlier work.

First, the troublesome double pole which appears in a quenched calculation of the quantity Λ_S because of topological near-zero modes is now highly suppressed by the $2 + 1$ flavor determinant. This allows us to use Λ_S for an accurate calculation of Z_m. Second we have identified the $O(5\%)$ large chiral symmetry breaking effects seen in the off-shell Green functions Λ_V and Λ_A as caused by our use of exceptional momenta. We have advanced both a theoretical discussion explaining the pattern of symmetry breaking which we have observed and a calculation with nonexceptional momenta in which these effects are dramatically reduced.

Third, for Z_{B_K} we have presented both a theoretical argument and numerical calculations showing the mixing coefficients with the operators with the wrong chirality are very small so that the calculation of Z_{B_K} can be simplified by neglecting these mixing coefficients. Finally, we have exploited the earlier perturbative work of others and evaluated the factors relating the normalization of operators defined in the $\overline{\mathrm{MS}}$ and RI/MOM schemes determining $Z_m^{\overline{\mathrm{MS}}}$, $Z_q^{\overline{\mathrm{MS}}}$, $Z_{B_K}^{\overline{\mathrm{MS}}}$ and $Z_T^{\overline{\mathrm{MS}}}$ from their nonperturbative RI/MOM counterparts to three, three, one and two loops, respectively.

ACKNOWLEDGMENTS

We thank our collaborators in the RBC and UKQCD collaborations for assistance and useful discussions. This work was supported by DOE Grant No. DE-FG02-

92ER40699 and PPARC Grant Nos. PPA/G/O/2002/00465 and PP/D000238/1. We thank the University of Edinburgh, PPARC, RIKEN, BNL, and the U.S. DOE for providing the facilities on which this work was performed. A. S. was supported by the U.S. Department of Energy under Contract Nos. DE-AC02-98CH10886, and DE-FG02-92ER40716.

APPENDIX A: THE QCD β FUNCTIONS AND THE RUNNING OF α_s

The four-loop QCD beta functions is calculated in [25] and the conventions we use are the same as in [15]:

$$\begin{aligned}\beta_0 &= \tfrac{1}{4}(11 - \tfrac{2}{3}n_f),\\ \beta_1 &= \tfrac{1}{16}(102 - \tfrac{38}{3}n_f),\\ \beta_2 &= \tfrac{1}{64}(\tfrac{2857}{2} - \tfrac{5033}{18}n_f + \tfrac{325}{54}n_f^2),\\ \beta_3 &= \tfrac{1}{256}[\tfrac{149\,753}{6} + 3564\zeta_3 - (\tfrac{1\,078\,361}{162} + \tfrac{6508}{27}\zeta_3)n_f\\ &\quad + (\tfrac{50\,065}{162} + \tfrac{6472}{81}\zeta_3)n_f^2 + \tfrac{1093}{729}n_f^3].\end{aligned} \tag{A1}$$

To calculate the coupling constant $\alpha_s(\mu)$ at any scale, we have used the four-loop (NNNLO) running formula for α_s [25]:

$$\begin{aligned}\frac{\partial a_s}{\partial \ln \mu^2} &= \beta(a_s)\\ &= -\beta_0 a_s^2 - \beta_1 a_s^3 - \beta_2 a_s^4 - \beta_3 a_s^5 + \mathcal{O}(a_s^6)\end{aligned} \tag{A2}$$

where $a_s = \alpha_s/\pi$. (We have changed the normalization of a_s to match the definition of the β-functions coefficients.) For a numerical implementation, we start from the world-average value at $\mu = M_Z$ [26],

$$\alpha_s^{(5)}(M_Z) = 0.1176 \pm 0.002, \tag{A3}$$

where the superscript indicates that it is in the 5-flavor region, and run α_s across the m_b and m_c threshold with the matching conditions:

$$\alpha_s^{(5)}(m_b) = \alpha_s^{(4)}(m_b) \quad \text{and} \quad \alpha_s^{(4)}(m_c) = \alpha_s^{(3)}(m_c). \tag{A4}$$

Having computed $\alpha_s^{(3)}(m_c)$, we can calculate the coupling constant at any scale in the 3-flavor theory. For example,

$$\alpha_s^{(3)}(\mu = 2\ \text{GeV}) = 0.2904. \tag{A5}$$

APPENDIX B: PERTURBATIVE RUNNING AND MATCHING FOR Z_m

In [15], the renormalization group equation for $m_{\text{ren}}(\mu)$ is solved to four-loop order (NNNLO). Using the solution with our definition of the renormalization coefficients Z_m, we obtain

$$Z_m^{\text{SI}} = \frac{c(\alpha_s(\mu_0)/\pi)}{c(\alpha_s(\mu)/\pi)} Z_m^{\text{RI/MOM}}(\mu) \tag{B1}$$

where the function $c(x)$ is given by

$$\begin{aligned}c(x) = (x)^{\bar\gamma_0}\{1 &+ (\bar\gamma_1 - \bar\beta_1\bar\gamma_0)x + \tfrac{1}{2}[(\bar\gamma_1 - \bar\beta_1\bar\gamma_0)^2 + \bar\gamma_2\\ &+ \bar\beta_1^2\bar\gamma_0 - \bar\beta_1\bar\gamma_1 - \bar\beta_2\bar\gamma_0]x^2 + [\tfrac{1}{6}(\bar\gamma_1 - \bar\beta_1\bar\gamma_0)^3\\ &+ \tfrac{1}{2}(\bar\gamma_1 - \bar\beta_1\bar\gamma_0)(\bar\gamma_2 + \bar\beta_1^2\bar\gamma_0 - \bar\beta_1\bar\gamma_1 - \bar\beta_2\bar\gamma_0)\\ &+ \tfrac{1}{3}(\bar\gamma_3 - \bar\beta_1^3\bar\gamma_0 + 2\bar\beta_1\bar\beta_2\bar\gamma_0 - \bar\beta_3\bar\gamma_0 + \bar\beta_1^2\bar\gamma_1\\ &- \bar\beta_2\bar\gamma_1 - \bar\beta_1\bar\gamma_2)]x^3 + \mathcal{O}(x^4)\},\end{aligned} \tag{B2}$$

with $\bar\beta_i = \frac{\beta_i}{\beta_0}$ and

$$\bar\gamma_i = \frac{\gamma_m^{\text{RI/MOM}(i)}}{\beta_0} \tag{B3}$$

The evaluation of the coefficients of the QCD β function and the running of α_s are explained in Appendix A and the anomalous dimensions are

$$\begin{aligned}\gamma_m^{\text{RI/MOM}(0)} &= 1\\ \gamma_m^{\text{RI/MOM}(1)} &= \tfrac{1}{16}(126 - \tfrac{52}{9}n_f)\\ \gamma_m^{\text{RI/MOM}(2)} &= \tfrac{1}{64}[(\tfrac{20\,911}{3} - \tfrac{3344}{3}\zeta_3) + (-\tfrac{18\,386}{27} + \tfrac{128}{9}\zeta_3)n_f + \tfrac{928}{81}n_f^2]\\ \gamma_m^{\text{RI/MOM}(3)} &= \tfrac{1}{256}[(\tfrac{300\,665\,987}{648} - \tfrac{15\,000\,871}{108}\zeta_3 + \tfrac{6160}{3}\zeta_5) + (-\tfrac{7\,535\,473}{108} + \tfrac{627\,127}{54}\zeta_3 + \tfrac{4160}{3}\zeta_5)n_f + (\tfrac{670\,948}{243} - \tfrac{6416}{27}\zeta_3)n_f^2 - \tfrac{18\,832}{729}n_f^3],\end{aligned} \tag{B4}$$

where $n_f = 3$.

When applying Eq. (B1), we need to choose a value of μ_0, where the SI value is calculated. The exact value of μ_0 is immaterial and for convenience we choose its value such that

$$(a\mu_0)^2 = 2. \tag{B5}$$

To match the renormalization coefficients Z_m from RI/MOM scheme to $\overline{\text{MS}}$ scheme, we have applied the three-loop matching factor [15] obtaining:

$$\frac{Z_m^{\overline{\rm MS}}}{Z_m^{\rm RI/MOM}} = 1 + \frac{\alpha_s}{4\pi}\left[-\frac{16}{3}\right] + \left(\frac{\alpha_s}{4\pi}\right)^2\left[-\frac{1990}{9} + \frac{152}{3}\zeta_3 + \frac{89}{9}n_f\right] + \left(\frac{\alpha_s}{4\pi}\right)^3\left[-\frac{6\,663\,911}{648} + \frac{408\,007}{108}\zeta_3 - \frac{2960}{9}\zeta_5 + \frac{236\,650}{243}n_f - \frac{4936}{27}\zeta_3 n_f + \frac{80}{3}\zeta_4 n_f - \frac{8918}{729}n_f^2 - \frac{32}{27}\zeta_3 n_f^2\right]. \tag{B6}$$

APPENDIX C: PERTURBATIVE RUNNING AND SCHEME MATCHING FOR Z_q

The renormalization group equation for Z_q is very similar to that for Z_m [15] and we can reuse the solution of the equation from Appendix B to write:

$$Z_q^{\rm SI} = \frac{c^{[\gamma_2]}(\alpha_s(\mu_0)/\pi)}{c^{[\gamma_2]}(\alpha_s(\mu)/\pi)} Z_q^{\rm RI/MOM}(\mu) \tag{C1}$$

where the function $c^{[\gamma_2]}(x)$ has exactly the same functional form as $c(x)$ defined in Eq. (B2), but with the coefficients $\bar{\gamma}_i$ of the anomalous dimension γ_m replaced by those of γ_2:

$$\bar{\gamma}_i = \frac{\gamma_2^{\rm RI/MOM(}i\rm)}{\beta_0} \tag{C2}$$

The coefficients of the anomalous dimension γ_2 are [15]

$$\begin{aligned}
\gamma_2^{\rm RI/MOM(0)} &= 0 \\
\gamma_2^{\rm RI/MOM(1)} &= \frac{N^2-1}{16N^2}\left\{\left[\frac{3}{8} + \frac{11}{4}N^2\right] + n_f\left[-\frac{1}{2}N\right]\right\} \\
\gamma_2^{\rm RI/MOM(2)} &= \frac{N^2-1}{64N^3}\left\{\left[\frac{3}{16} + \frac{25}{3}N^2 + \frac{14\,225}{288}N^4 - 3N^2\zeta_3 - \frac{197}{16}N^4\zeta_3\right] + n_f\left[-\frac{1}{3}N - \frac{611}{36}N^3 + 2N^3\zeta_3\right] + n_f^2\left[\frac{10}{9}N^2\right]\right\} \\
\gamma_2^{\rm RI/MOM(3)} &= \frac{N^2-1}{256N^4}\left\{\left[\frac{1027}{128} + \frac{7673}{384}N^2 + \frac{174\,565}{1152}N^4 + \frac{3\,993\,865}{3456}N^6 + 25\zeta_3 + 31N^2\zeta_3 - \frac{10\,975}{64}N^4\zeta_3 - \frac{111\,719}{192}N^6\zeta_3\right.\right. \\
&\quad - 40\zeta_5 - 60N^2\zeta_5 + \frac{5465}{64}N^4\zeta_5 + \frac{20\,625}{128}N^6\zeta_5\Big] + n_f\left[\frac{1307}{48}N + \frac{557}{144}N^3 - \frac{172\,793}{288}N^5 - 4N\zeta_3 + 2N^3\zeta_3\right. \\
&\quad \left.\left. + \frac{7861}{48}N^5\zeta_3 - 30N^3\zeta_5 - \frac{125}{4}N^5\zeta_5\right] + n_f^2\left[-\frac{521}{72}N^2 + \frac{259}{3}N^4 + 6N^2\zeta_3 - \frac{26}{3}N^4\zeta_3\right] + n_f^3\left[-\frac{86}{27}N^3\right]\right\}
\end{aligned} \tag{C3}$$

where $N = 3$, which represents the number of colors, and $n_f = 3$.

When we match Z_q from RI/MOM scheme to $\overline{\rm MS}$ scheme, the three-loop matching factor is [15]

$$\frac{Z_q^{\overline{\rm MS}}}{Z_q^{\rm RI/MOM}} = 1 + \left(\frac{\alpha_s}{4\pi}\right)^2\left[-\frac{517}{18} + 12\zeta_3 + \frac{5}{3}n_f\right] + \left(\frac{\alpha_s}{4\pi}\right)^3\left[-\frac{1\,287\,283}{648} + \frac{14\,197}{12}\zeta_3 + \frac{79}{4}\zeta_4 - \frac{1165}{3}\zeta_5 + \frac{18\,014}{81}n_f - \frac{368}{9}\zeta_3 n_f - \frac{1102}{243}n_f^2\right]. \tag{C4}$$

APPENDIX D: PERTURBATIVE RUNNING AND SCHEME MATCHING FOR Z_{B_K}

To remove (restore) the perturbative renormalization group running of Z_{B_K}, we use the one-loop renormalization group running formula [16]:

$$Z_{B_K}^{\rm SI}(n_f) = w_{\rm scheme}^{-1}(\mu, n_f) Z_{B_K}^{\rm scheme}(\mu, n_f) \tag{D1}$$

where

$$w_{\rm scheme}^{-1}(\mu, n_f) = \alpha_s(\mu)^{-\gamma_0/2\beta_0}\left[1 + \frac{\alpha_s(\mu)}{4\pi}J_{\rm scheme}^{(n_f)}\right] \tag{D2}$$

and

$$J_{\rm RI/MOM}^{(n_f)} = -\frac{17397 - 2070n_f + 104n_f^2}{6(33-2n_f)^2} + 8\ln 2 \tag{D3}$$

$$J_{\overline{\rm MS}}^{(n_f)} = \frac{13\,095 - 1626n_f + 8n_f^2}{6(33-2n_f)^2} \tag{D4}$$

with $n_f = 3$ in our analysis.

APPENDIX E: PERTURBATIVE RUNNING AND SCHEME MATCHING FOR Z_T

The anomalous dimension of the tensor current in the $\overline{\text{MS}}$ scheme is given at three-loops in [27],

$$\begin{aligned}\gamma_T^{\overline{\text{MS}}(0)} &= \tfrac{1}{3},\\ \gamma_T^{\overline{\text{MS}}(1)} &= \tfrac{1}{16}\tfrac{2}{27}(543 - 26n_f),\\ \gamma_T^{\overline{\text{MS}}(2)} &= \tfrac{1}{64}\tfrac{2}{243}(\tfrac{1}{2}157\,665 - 4176\zeta_3\\ &\quad - (2160\zeta_3 + 7860)n_f - 54n_f^2).\end{aligned} \tag{E1}$$

For consistency we have adjusted the normalization from that used in [27] such that $\gamma_T^{\overline{\text{MS}}}$ satisfies the generic RG-equation for the renormalization constant Z_Γ of the quark bilinear $\bar\psi\Gamma\psi$,

$$\frac{\partial \ln Z_\Gamma}{\partial \ln \mu^2} = \gamma_\Gamma(a_s) = -\gamma_\Gamma^{(0)} a_s - \gamma_\Gamma^{(1)} a_s^2 - \gamma_\Gamma^{(2)} a_s^3 + \mathcal{O}(a_s^4), \tag{E2}$$

with $a_s = \alpha_s/\pi$.

The perturbative running for the tensor current has also been computed at three loops in the RI/MOM′ scheme [27], and we use it to obtain the RI/MOM scheme anomalous dimension as follows. We consider the conversion function $C_\Gamma^{\text{RI/MOM}^{(\prime)}}$ used to match the RI/MOM or RI/MOM′ scheme to the $\overline{\text{MS}}$ scheme:

$$Z_\Gamma^{\overline{\text{MS}}} = C_\Gamma^{\text{RI/MOM}^{(\prime)}} Z_\Gamma^{\text{RI/MOM}^{(\prime)}}. \tag{E3}$$

Applying the above renormalization group Eq. (E2) we obtain

$$\gamma_\Gamma^{\text{RI/MOM}^{(\prime)}} = \gamma_\Gamma^{\overline{\text{MS}}} - \frac{\partial \ln C_\Gamma^{\text{RI/MOM}^{(\prime)}}}{\partial \ln \mu^2}. \tag{E4}$$

Since the only difference between the RI/MOM and RI/MOM′ schemes lies in the definition of the quark field renormalization constants $Z_2^{\text{RI/MOM}'}$ and $Z_2^{\text{RI/MOM}}$, we write $C_\Gamma^{\text{RI/MOM}^{(\prime)}} = C_\Gamma C_2^{\text{RI/MOM}^{(\prime)}}$. The vertex part C_Γ of the conversion function is common to both the RI/MOM and RI/MOM′ schemes. It follows that

$$\begin{aligned}\gamma_\Gamma^{\text{RI/MOM}'} - \gamma_\Gamma^{\text{RI/MOM}} &= \frac{\partial \ln C_2^{\text{RI/MOM}}}{\partial \ln \mu^2} - \frac{\partial \ln C_2^{\text{RI/MOM}'}}{\partial \ln \mu^2}\\ &= \gamma_2^{\text{RI/MOM}} - \gamma_2^{\text{RI/MOM}'}.\end{aligned} \tag{E5}$$

Since both functions $\gamma_2^{\text{RI/MOM}}$ and $\gamma_2^{\text{RI/MOM}'}$ are known [15], we can now compute the anomalous dimension of the tensor current in the RI/MOM scheme from the known one in the RI/MOM′ scheme. We note that since the r.h.s. of (E5) is valid for any choice of Γ on the l.h.s., one may use the identity

$$\gamma_\Gamma^{\text{RI/MOM}} = \gamma_\Gamma^{\text{RI/MOM}'} - (\gamma_{\Gamma'}^{\text{RI/MOM}'} - \gamma_{\Gamma'}^{\text{RI/MOM}}). \tag{E6}$$

In order to compute $\gamma_T^{\text{RI/MOM}}$ here we have used $\gamma_2^{\text{RI/MOM}}$ as in (C2) and $\gamma_2^{\text{RI/MOM}'}$ from [15]:

$$\begin{aligned}\gamma_2^{\text{RI/MOM}'(0)} &= 0,\\ \gamma_2^{\text{RI/MOM}'(1)} &= \frac{N^2-1}{16N^2}\left\{\left[\frac{3}{8} + \frac{11}{4}N^2\right] + n_f\left[-\frac{1}{2}N\right]\right\},\\ \gamma_2^{\text{RI/MOM}'(2)} &= \frac{N^2-1}{64N^3}\left\{\left[\frac{3}{16} + \frac{233}{24}N^2 + \frac{17\,129}{288}N^4 - 3N^2\zeta_3 - \frac{197}{16}N^4\zeta_3\right] + n_f\left[-\frac{7}{12}N - \frac{743}{36}N^3 + 2N^3\zeta_3\right]\right.\\ &\quad \left. + n_f^2\left[\frac{13}{9}N^2\right]\right\},\\ \gamma_2^{\text{RI/MOM}'(3)} &= \frac{N^2-1}{256N^4}\left\{\left[\frac{1027}{128} + \frac{8069}{384}N^2 + \frac{240\,973}{1152}N^4 + \frac{5\,232\,091}{3456}N^6 + 25\zeta_3 + 31N^2\zeta_3 - \frac{12\,031}{64}N^4\zeta_3 - \frac{124\,721}{192}N^6\zeta_3\right.\right.\\ &\quad - 40\zeta_5 - 60N^2\zeta_5 + \frac{5465}{64}N^4\zeta_5 + \frac{20\,625}{128}N^6\zeta_5\Big] + n_f\left[\frac{329}{12}N - \frac{1141}{144}N^3 - \frac{113\,839}{144}N^5 - 4N\zeta_3 + 5N^3\zeta_3\right.\\ &\quad \left.\left. + \frac{2245}{12}N^5\zeta_3 - 30N^3\zeta_5 - \frac{125}{4}N^5\zeta_5\right] + n_f^2\left[-\frac{515}{72}N^2 + \frac{1405}{12}N^4 + 6N^2\zeta_3 - \frac{32}{3}N^4\zeta_3\right] + n_f^3\left[-\frac{125}{27}N^3\right]\right\}.\end{aligned} \tag{E7}$$

In this way we obtain the anomalous dimension:

$$\begin{aligned}\gamma_T^{\text{RI/MOM}(0)} &= \tfrac{1}{3}, \qquad \gamma_T^{\text{RI/MOM}(1)} = \tfrac{1}{16}\tfrac{2}{27}(543 - 26n_f),\\ \gamma_T^{\text{RI/MOM}(2)} &= \tfrac{1}{64}\tfrac{1}{243}(478\,821 - 117\,648\zeta(3) + 6(384\zeta(3) - 8713)n_f + 928n_f^2),\end{aligned} \tag{E8}$$

from which we compute the running of Z_T using (B2).

Combining (A2) and (E2) we compute the expression for the matching factor $C_T^{\mathrm{RI/MOM}}$. After expanding in a_s we obtain:

$$\frac{Z_T^{\overline{\mathrm{MS}}}}{Z_T^{\mathrm{RI/MOM}}} = 1 + \frac{1}{81}(-4866 + 1656\zeta(3) + 259n_f)\left(\frac{\alpha_s}{4\pi}\right)^2. \tag{E9}$$

[1] D. J. Antonio *et al.* (RBC and UKQCD), Phys. Rev. D **75**, 114501 (2007).
[2] C. Allton *et al.* (RBC and UKQCD), Phys. Rev. D **76**, 014504 (2007).
[3] P. Boyle (RBC), Proc. Sci. Lat2007 (2007) 005 [arXiv:0710.5880].
[4] G. Martinelli, C. Pittori, C. T. Sachrajda, M. Testa, and A. Vladikas, Nucl. Phys. **B445**, 81 (1995).
[5] M. Lin and E. E. Scholz (RBC and UKQCD), Proc. Sci. LATTICE2007 (2007) 120 [arXiv:0710.0536].
[6] S. Aoki, T. Izubuchi, Y. Kuramashi, and Y. Taniguchi, Phys. Rev. D **67**, 094502 (2003).
[7] S. Aoki and Y. Kuramashi, Phys. Rev. D **68**, 034507 (2003).
[8] T. Blum *et al.*, Phys. Rev. D **66**, 014504 (2002).
[9] N. Christ (RBC and UKQCD), Proc. Sci., LAT2005 (2006) 345.
[10] S. Weinberg, Phys. Rev. **118**, 838 (1960).
[11] C. Itzykson and J. B. Zuber, *International Series in Pure and Applied Physics* (McGraw-Hill, New York, 1980), p. 705.
[12] V. Furman and Y. Shamir, Nucl. Phys. **B439**, 54 (1995).
[13] H. D. Politzer, Nucl. Phys. **B117**, 397 (1976).
[14] D. Becirevic, V. Gimenez, V. Lubicz, and G. Martinelli, Phys. Rev. D **61**, 114507 (2000).
[15] K. G. Chetyrkin and A. Retey, Nucl. Phys. **B583**, 3 (2000).
[16] Y. Aoki *et al.*, Phys. Rev. D **73**, 094507 (2006).
[17] D. Becirevic, Nucl. Phys. B, Proc. Suppl. **129**, 34 (2004).
[18] D. J. Antonio *et al.*, Phys. Rev. D **77**, 014509 (2008).
[19] M. Golterman and Y. Shamir, Phys. Rev. D **68**, 074501 (2003).
[20] M. Golterman, Y. Shamir, and B. Svetitsky, Phys. Rev. D **71**, 071502 (2005).
[21] M. Golterman, Y. Shamir, and B. Svetitsky, Phys. Rev. D **72**, 034501 (2005).
[22] B. Svetitsky, Y. Shamir, and M. Golterman, Proc. Sci., LAT2005 (2006) 129.
[23] M. Golterman and Y. Shamir, Phys. Rev. D **71**, 034502 (2005).
[24] D. J. Antonio *et al.*, Phys. Rev. Lett. **100**, 032001 (2008).
[25] T. van Ritbergen, J. A. M. Vermaseren, and S. A. Larin, Phys. Lett. B **400**, 379 (1997).
[26] W. M. Yao *et al.* (Particle Data Group), J. Phys. G **33**, 1 (2006).
[27] J. A. Gracey, Nucl. Phys. **B662**, 247 (2003).
[28] C. Dawson (RBC), Nucl. Phys. B, Proc. Suppl. **119**, 314 (2003).
[29] Y. Aoki, C. Dawson, J. Noaki, and A. Soni, Phys. Rev. D **75**, 014507 (2007).